Skid steering-based control of a robotic vehicle with six in-wheel drives

J Kang[1], **W Kim**[2], **J Lee**[3], and **K Yi**[1]*
[1]School of Mechanical and Aerospace Engineering, Seoul National University, Seoul, Republic of Korea
[2]Program in Automotive Engineering, Seoul National University, Seoul, Republic of Korea
[3]Samsung Techwin, Gyeongsang-do, Republic of Korea

The manuscript was received on 9 October 2009 and was accepted after revision for publication on 18 May 2010.

DOI: 10.1243/09544070JAUTO1405

Abstract: This paper describes a driving control algorithm based on a skid steering for a robotic vehicle with articulated suspension (RVAS). The RVAS is a kind of unmanned ground vehicle based on a skid steering using an independent in-wheel drive at each wheel. The driving control algorithm consists of four parts: a speed controller for following a desired speed, a lateral motion controller that computes a yaw moment input to track a desired yaw rate or a desired trajectory according to the control mode, a longitudinal tyre force distribution algorithm that determines an optimal desired longitudinal tyre force, and a wheel torque controller that determines a wheel torque command at each wheel in order to keep the slip ratio at each wheel below a limit value as well as to track the desired tyre force. Longitudinal and vertical tyre force estimators are required for the optimal tyre force distribution and wheel slip control. A dynamic model of the RVAS for simulation study is developed and validated using the vehicle test data. Simulation and vehicle tests are conducted in order to evaluate the proposed driving controller. It is found from simulation and vehicle test results that the proposed driving controller provides a satisfactory motion control performance according to the control mode.

Keywords: skid steering vehicle, manoeuvrability, driving controller, tyre force distribution, wheel torque control

1 INTRODUCTION

Recently, diverse unmanned ground vehicles have been developed in order to conduct multi-tasks such as logistics supports, surveillance, and light combat operation. In this paper, as part of the autonomous vehicle control for a military or robotic vehicle, a skid steering-based driving control algorithm is investigated. A robotic vehicle with articulated suspension (RVAS), as shown in Fig. 1, is a kind of unmanned ground vehicle based on a skid steering using independent in-wheel drive at each wheel. The RVAS, unlike the conventional wheeled vehicles, is not equipped with steering linkages. Instead, it is steered by means of differential traction force which is created from an in-wheel motor at each wheel. Steering in this way requires much more power consumption than does kinematic steering using Ackerman's linkages. However, this offers a simple structure and more room in the vehicle for the instalment of mission equipment. From the mobility aspect, the RVAS benefits from its in-wheel drives and articulated suspensions, which provide an independent wheel traction control capability and a great improvement in obstacle negotiation ability respectively.

In this paper, the driving control algorithm based on skid steering of the RVAS is investigated in order to control the vehicle motion according to the remote driver's command or to track a prescribed trajectory. The proposed driving control algorithm is related to many research topics such as the motion control of the skid-steering vehicle, vehicle dynamic control for manoeuvrability, and trajectory tracking control.

*Corresponding author: Mechanical and Aerospace Engineering, Seoul National University, Kwanak-ku, Shillim-dong 56-1, Seoul, 151-792, Republic of Korea.
email: kyi@snu.ac.kr

Fig. 1 Robotic vehicle with articulated suspension (RVAS)

Diverse control strategies for a skid-steering vehicle have been proposed in earlier research. Golconda presented the steering controller of a six-wheeled vehicle based on skid steering. The steering controller consists of a proportional–integral–derivative (PID) controller with two filters: a prediction filter and a safety filter [**1**]. Economou and Colyer proposed fuzzy logic control of wheeled skid-steer electric vehicles [**2**]. Dixon *et al.* investigated the non-linear control of wheeled mobile robots [**3**]. Also, there has been some research on vehicle dynamic control for manoeuvrability. Cho *et al.* investigated a unified chassis control scheme for optimized vehicle stability and manoeuvrability [**4**]. Yi *et al.* proposed differential braking strategies for vehicle stability control [**5**]. Uematsu and Gerdes designed and compared diverse sliding mode controllers for vehicle dynamic control [**6**]. Chen and Peng evaluated the vehicle dynamic control algorithm based on differential braking [**7**]. Finally, research relating to trajectory tracking has been carried out for several decades. Kang *et al.* designed and tested a controller for autonomous vehicle path tracking using GPS/INS sensors [**8**]. Peng proposed a path-tracking controller based on the optimal finite preview control method [**9**]. Lenain *et al.* introduced a non-linear adaptive control law in order to preserve guidance precision in the presence of sliding [**10**]. Lizarralde *et al.* presented a method for mobile robot navigation where dead-reckoning data is combined with range-sensor data via a Kalman filter to provide input to a non-linear model predictive control (NMPC) algorithm [**11**]. However, since these researches were conducted for a conventional suspension vehicle, the articulated suspension vehicle such as the RVAS is not applicable.

This paper is organized in the following manner. A dynamic model for the RVAS is developed and validated in section 2 using the test data. In section 3, the overall control strategy based on a skid steering is presented. In this section, an upper-level controller and a lower-level controller are designed for vehicle motion control according to the control mode. The longitudinal and vertical tyre forces are estimated in section 4. Simulation and vehicle tests are conducted in order to evaluate the proposed driving controller, and the test results are compared with the simulation results in sections 5 and 6. Finally, section 7 concludes this paper.

2 DYNAMIC MODEL OF A VEHICLE WITH SIX INDEPENDENT IN-WHEEL DRIVES

A full dynamic model of the RVAS is developed to conduct numerical simulation studies as shown in Fig. 2. The dynamic model has 18 degrees of freedom (DOF) with the dynamic equations of sprung mass, six arm rods, and six wheels. The dynamic motion of sprung mass is modelled as 6DOF, including translational motions (longitudinal, lateral, vertical) and rotational motions (roll, pitch, yaw). The sprung mass is assumed as a rigid body connected with the six arm rods.

2.1 Development of vehicle dynamic model

The full dynamic model of the RVAS is designed as having three parts: driving system, arm dynamic model, and vehicle body dynamic model, as shown in Fig. 3. The driving system contains an in-wheel motor model, a wheel dynamic model, and a tyre model. The arm dynamic model determines the dynamic behaviours of the *i*th arm rod. The vehicle body dynamic model is designed to represent the dynamic behaviour of a sprung mass. The numerical values are listed in Table 1.

2.1.1 Driving system

The driving system in the dynamic model consists of an in-wheel motor model, a wheel dynamic model, and a tyre model. The in-wheel motor is modelled using a first-order transfer function. The torque/speed curve as shown in Fig. 4 is used to consider the maximum power of the in-wheel motor in the dynamic model of the RVAS.

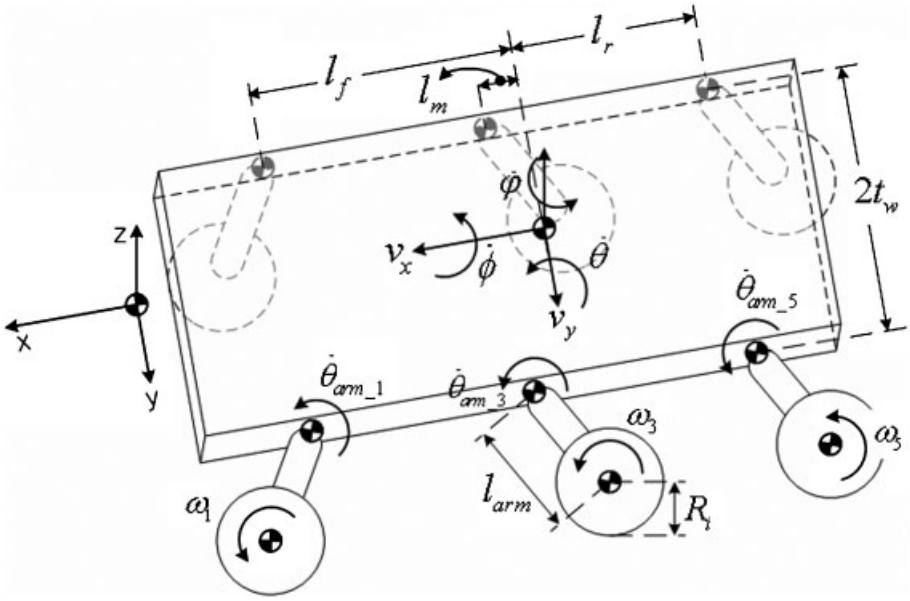

Fig. 2 18DOF full dynamic model of robotic vehicle with articulated suspension

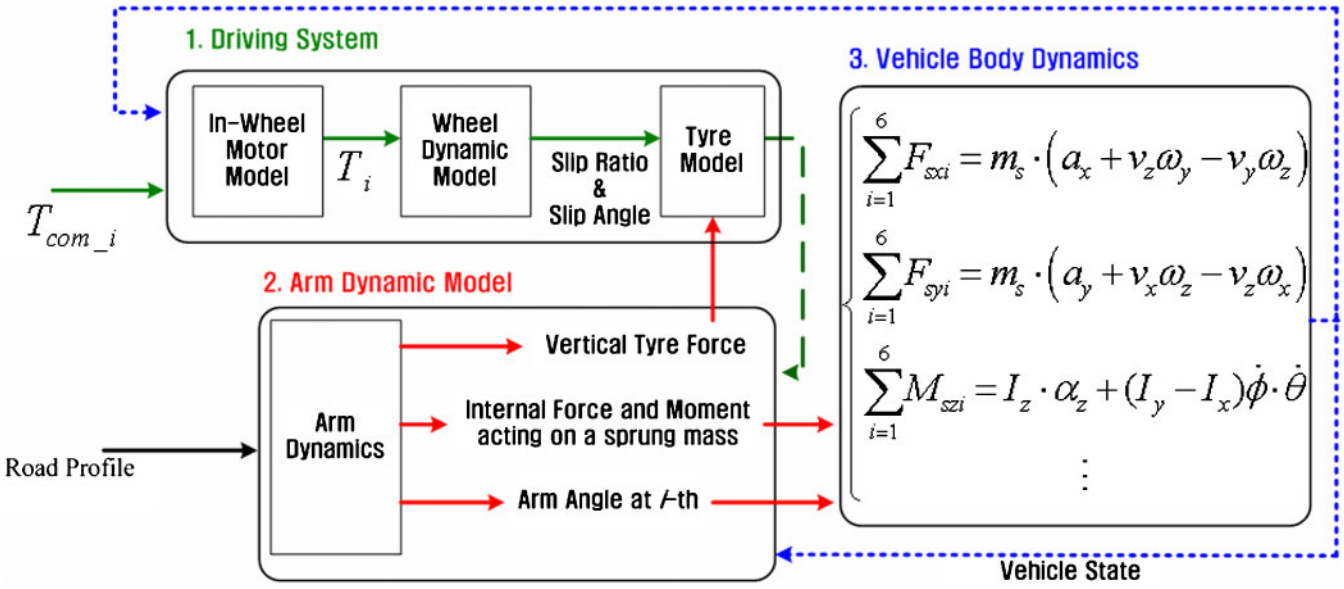

Fig. 3 Schematic diagram of the dynamic model

Table 1 Parameters of vehicle dynamic model

Symbol	Value	Symbol	Value
m	1500 kg	l_r	−0.76 m
m_{arm}	31.7 kg	l_{arm}	0.42 m
m_s	1002 kg	I_x	460 kg m^2
m_w	51.3 kg	I_y	900 kg m^2
l_f	0.92 m	I_z	1200 kg m^2
l_m	0.08 m	t_w	0.8085 m

The wheel dynamic model can be designed using the wheel dynamic equation

$$J_w \times \frac{d\omega_i(t)}{dt} = T_i(t) \times R_i F_{txi}(t) \quad (1)$$

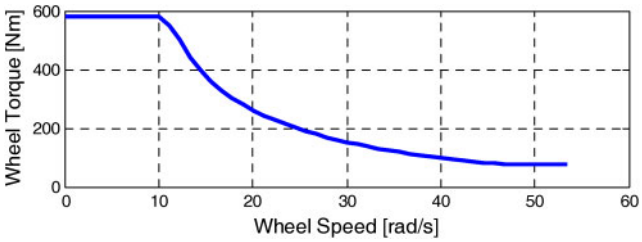

Fig. 4 Torque/speed curve of each in-wheel motor

Finally, longitudinal and lateral tyre models are modelled using a combined Pacejka tyre model [**12**]. The tyre forces are related to wheel slip ratio and slip

angle. The wheel slip ratio and the slip angle are defined as in equation (2)

$$\lambda_i = \begin{cases} \dfrac{R_i \times \omega_i - v_{txi}}{R_i \cdot \omega_i} & \text{if } (\lambda_i > 0) \\ \dfrac{R_i \times \omega_i - v_{txi}}{v_{txi}} & \text{if } (\lambda_i \leqslant 0) \end{cases}, \quad \alpha_i = -\tan^{-1}\left(\frac{v_{tyi}}{v_{txi}}\right) \tag{2}$$

where v_{txi} and v_{tyi} denote the longitudinal and lateral velocity at the tyre centre and can be calculated as

$$\begin{aligned} \dot{r}_{wi} &= \begin{bmatrix} v_{txi} & v_{tyi} & v_{tzi} \end{bmatrix}^{\mathrm{T}} \\ &= \dot{r}_{cg} + \omega_{cg} \times r_{i/cg} + \omega_{arm\_i/cg} \times r_{wi/i} \\ &= \overbrace{\begin{bmatrix} v_x \\ v_y \\ v_z \end{bmatrix}}^{\dot{r}_{cg}} + \overbrace{\begin{bmatrix} \dot{\phi} \\ \dot{\theta} \\ \dot{\varphi} \end{bmatrix}}^{\omega_{cg}} \times \overbrace{\begin{bmatrix} l_i \\ \pm t_w \\ 0 \end{bmatrix}}^{r_{i/cg}} \\ &\quad + \overbrace{\begin{bmatrix} 0 \\ \dot{\theta}_{arm\_i} \\ 0 \end{bmatrix}}^{\omega_{arm\_i/cg}} \times \overbrace{\begin{bmatrix} -l_{arm} \times \sin(\theta_{arm\_i}) \\ 0 \\ -l_{arm} \times \cos(\theta_{arm\_i}) \end{bmatrix}}^{r_{wi/i}} \end{aligned} \tag{3}$$

where $\dot{r}_{cg}$ denotes the vehicle velocity vector, ω_{cg} the vehicle angular velocity vector, $r_{i/cg}$ the distance vector from the centre of gravity (c.g.) to the rotational centre of the ith arm rod, $r_{wi/i}$ the distance vector from the rotational centre of the ith arm rod to the ith wheel, and $\omega_{arm\_i/cg}$ the relative angular velocity vector of the ith arm rod to the rotational centre of the ith arm rod respectively.

2.1.2 *Arm dynamic model*

The arm dynamic model determines the arm behaviour of each arm rod and internal forces and moments acting on a sprung mass. The behaviour of each arm rod occurs due to longitudinal, lateral, and vertical tyre forces and arm spring and damping torques. Figure 5 shows the dynamic equilibrium of the ith arm rod.

From Fig. 5, the dynamic equations for the arm dynamic model can be expressed as follows

$$\begin{aligned} \sum F_{x\_arm\_i} &= F_{txi} - F_{sxi} = (m_{arm} \times \ddot{x}_{arm\_i}) + (m_w \times \ddot{x}_{w\_i}) \\ \sum F_{y\_arm\_i} &= F_{tyi} - F_{syi} = (m_{arm} \times \ddot{y}_{arm\_i}) + (m_w \times \ddot{y}_{w\_i}) \\ \sum F_{z\_arm\_i} &= F_{tzi} - F_{szi} - (m_w + m_{arm}) \cdot g \\ &= (m_{arm} \times \ddot{z}_{arm\_i}) + (m_w \times \ddot{z}_{w\_i}) \end{aligned} \tag{4}$$

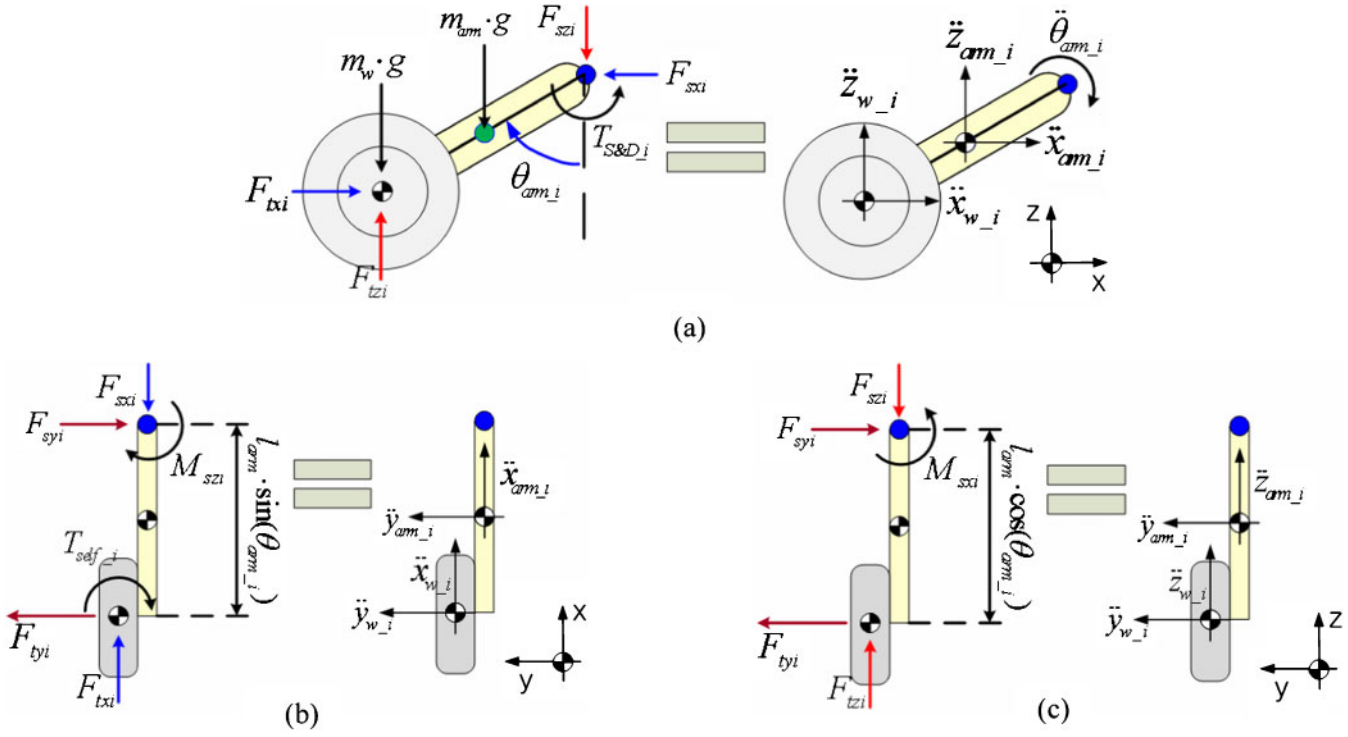

Fig. 5 Dynamic equilibrium of ith arm rod, (a) right-side view, (b) top view, and (c) rear view

$$\begin{aligned}
\sum M_{x_\mathrm{arm}_i} &= I_{\mathrm{arm}_x} \times \alpha_{\mathrm{arm}_xi} + \left(I_{\mathrm{arm}_z} - I_{\mathrm{arm}_y}\right) \times \omega_{\mathrm{arm}_yi} \times \omega_{\mathrm{arm}_zi} \\
&\quad + l_{\mathrm{arm}} \times \cos(\theta_{\mathrm{arm}_i}) \left(m_{\mathrm{w}} \times \ddot{y}_{wi} + m_{\mathrm{arm}} \frac{\ddot{y}_{\mathrm{arm}_i}}{2} \right) \\
\sum M_{y_\mathrm{arm}_i} &= I_{\mathrm{arm}_y} \times \alpha_{\mathrm{arm}_yi} + (I_{\mathrm{arm}_x} - I_{\mathrm{arm}_z}) \omega_{\mathrm{arm}_zi} \times \omega_{\mathrm{arm}_xi} \\
&\quad - \left(m_{\mathrm{w}} \times \ddot{x}_{\mathrm{w}i} + m_{\mathrm{arm}} \frac{\ddot{x}_{\mathrm{arm}_i}}{2} \right) l_{\mathrm{arm}} \times \cos(\theta_{\mathrm{arm}_i}) + \left(m_{\mathrm{w}} \times \ddot{z}_{\mathrm{w}i} + m_{\mathrm{arm}} \frac{\ddot{z}_{\mathrm{arm}_i}}{2} \right) \times l_{\mathrm{arm}} \times \sin(\theta_{\mathrm{arm}_i}) \\
\sum M_{z_\mathrm{arm}_i} &= I_{\mathrm{arm}_z} \times \alpha_{\mathrm{arm}_zi} + \left(I_{\mathrm{arm}_y} - I_{\mathrm{arm}_x}\right) \omega_{\mathrm{arm}_xi} \times \omega_{\mathrm{arm}_yi} \\
&\quad - l_{\mathrm{arm}} \times \sin(\theta_{\mathrm{arm}_i}) \left(m_{\mathrm{w}} \times \ddot{y}_{\mathrm{w}i} + m_{\mathrm{arm}} \frac{\ddot{y}_{\mathrm{arm}_i}}{2} \right)
\end{aligned} \tag{5}$$

In equations (4) and (5), the angular velocity vector of the ith arm rod, ω_{arm_i}, the angular acceleration vector of the ith arm rod, α_{arm_i}, and the translational acceleration vector of the ith wheel, $\ddot{r}_{wi}$, are given as shown in equations (6) to (8) [**13**]

$$\begin{aligned}
\omega_{\mathrm{arm}_i} &= \begin{bmatrix} \omega_{\mathrm{arm}_xi} & \omega_{\mathrm{arm}_yi} & \omega_{\mathrm{arm}_zi} \end{bmatrix}^{\mathrm{T}} \\
&= \omega_{\mathrm{cg}} + \omega_{\mathrm{arm}_i/\mathrm{cg}} = \begin{bmatrix} \dot{\phi} & \dot{\theta} + \dot{\theta}_{\mathrm{arm}_i} & \dot{\varphi} \end{bmatrix}^{\mathrm{T}}
\end{aligned} \tag{6}$$

$$\begin{aligned}
\alpha_{\mathrm{arm}_i} &= \begin{bmatrix} \alpha_{\mathrm{arm}_xi} & \alpha_{\mathrm{arm}_yi} & \alpha_{\mathrm{arm}_zi} \end{bmatrix}^{\mathrm{T}} \\
&= \alpha_{\mathrm{cg}} + \alpha_{\mathrm{arm}_i/\mathrm{cg}} + \omega_{\mathrm{cg}} \times \omega_{\mathrm{arm}_i/\mathrm{cg}} \\
&= \overbrace{\begin{bmatrix} \ddot{\phi} \\ \ddot{\theta} \\ \ddot{\varphi} \end{bmatrix}}^{\alpha_{\mathrm{cg}}} + \overbrace{\begin{bmatrix} 0 \\ \ddot{\theta}_{\mathrm{arm}_i} \\ 0 \end{bmatrix}}^{\alpha_{\mathrm{arm}_i/\mathrm{cg}}} + \overbrace{\begin{bmatrix} \dot{\phi} \\ \dot{\theta} \\ \dot{\varphi} \end{bmatrix}}^{\omega_{\mathrm{cg}}} \times \overbrace{\begin{bmatrix} 0 \\ \dot{\theta}_{\mathrm{arm}_i} \\ 0 \end{bmatrix}}^{\omega_{\mathrm{arm}_i/\mathrm{cg}}} \\
&= \begin{bmatrix} \ddot{\phi} - \dot{\theta}_{\mathrm{arm}_i} \times \dot{\varphi} \\ \ddot{\theta} + \ddot{\theta}_{\mathrm{arm}_i} \\ \ddot{\varphi} + \dot{\theta}_{\mathrm{arm}_i} \times \dot{\phi} \end{bmatrix}
\end{aligned} \tag{7}$$

$$\begin{aligned}
\ddot{r}_{\mathrm{w}i} &= \begin{bmatrix} \ddot{x}_{\mathrm{w}i} & \ddot{y}_{\mathrm{w}i} & \ddot{z}_{\mathrm{w}i} \end{bmatrix}^{\mathrm{T}} \\
&= \ddot{r}_i + \omega_{\mathrm{arm}_i} \times \left[\omega_{\mathrm{arm}_i} \times r_{\mathrm{w}i/i} \right] + \alpha_{\mathrm{arm}_i} \times r_{\mathrm{w}i/i} \\
\ddot{r}_i &= \begin{bmatrix} \ddot{x}_i & \ddot{y}_i & \ddot{z}_i \end{bmatrix}^{\mathrm{T}} \\
&= \ddot{r}_{\mathrm{cg}} + \omega_{\mathrm{cg}} \times \left[\omega_{\mathrm{cg}} \times r_{i/\mathrm{cg}} \right] + \alpha_{\mathrm{cg}} \times r_{i/\mathrm{cg}}
\end{aligned} \tag{8}$$

where α_{cg} denotes the vehicle angular acceleration vector, $\alpha_{\mathrm{arm}\_i/\mathrm{cg}}$ the relative angular acceleration vector of the ith arm rod to c.g., and $\ddot{r}_i$ the translational acceleration vector of the rotational centre of the ith arm rod respectively. The moment summations in equation (5) are shown in equation (9)

$$\begin{cases}
\sum M_{x_\mathrm{arm}_i} = -M_{sxi} + l_{\mathrm{arm}} \times \cos(\theta_{\mathrm{arm}_i}) \cdot F_{tyi} \\
\sum M_{y_\mathrm{arm}_i} = -T_{\mathrm{S\&D}_i} - l_{\mathrm{arm}} \times \sin(\theta_{\mathrm{arm}_i}) \left(m_{\mathrm{w}} + \dfrac{m_{\mathrm{arm}}}{2} \right) g \\
\qquad\qquad - l_{\mathrm{arm}} \times \cos(\theta_{\mathrm{arm}_i}) F_{txi} \\
\qquad\qquad + l_{\mathrm{arm}} \times \sin(\theta_{\mathrm{arm}_i}) F_{tzi} \\
\sum M_{z_\mathrm{arm}_i} = -M_{szi} - l_{\mathrm{arm}} \times \sin(\theta_{\mathrm{arm}_i}) F_{tyi} - T_{\mathrm{self}_i}
\end{cases} \tag{9}$$

where $T_{\mathrm{S\&D}\_i}$ denotes a sum of spring and damping torques of the ith arm rod as

$$T_{\mathrm{S\&D}\_i}\left(\theta_{\mathrm{arm}\_i}, \dot{\theta}_{\mathrm{arm}\_i}\right) = k_{\mathrm{s}} \times \theta_{\mathrm{arm}\_i} + c_{\mathrm{d}} \times \dot{\theta}_{\mathrm{arm}\_i} \tag{10}$$

Substituting equations (6) to (8) into equation (5), the dynamic equation for the arm motion can be obtained as

$$\begin{aligned}
&\left\{ I_{\mathrm{arm}_y} + \left(m_{\mathrm{w}} + \frac{m_{\mathrm{arm}}}{4} \right) l_{\mathrm{arm}}^2 \right\} \ddot{\theta}_{\mathrm{arm}_i} = \\
&\quad \sum M_{y_\mathrm{arm}_i} - \left\{ I_{\mathrm{arm}_y} + \left(m_{\mathrm{w}} + \frac{m_{\mathrm{arm}}}{4} \right) l_{\mathrm{arm}}^2 \right\} \ddot{\theta} \\
&\quad - (I_{\mathrm{arm}_x} - I_{\mathrm{arm}_z}) \dot{\phi} \dot{\varphi} \\
&\quad + \left(m_{\mathrm{w}} + \frac{m_{\mathrm{arm}}}{2} \right) l_{\mathrm{arm}} \{ \cos(\theta_{\mathrm{arm}_i}) \ddot{x}_i - \sin(\theta_{\mathrm{arm}_i}) \ddot{z}_i \} \\
&\quad - \left(m_{\mathrm{w}} + \frac{m_{\mathrm{arm}}}{4} \right) l_{\mathrm{arm}}^2 \left[\sin(\theta_{\mathrm{arm}_i}) \cos(\theta_{\mathrm{arm}_i}) \left(\dot{\phi}^2 - \dot{\varphi}^2 \right) \right. \\
&\quad \left. + \left\{ \cos^2(\theta_{\mathrm{arm}_i}) - \sin^2(\theta_{\mathrm{arm}_i}) \right\} \phi \dot{\varphi} \right]
\end{aligned} \tag{11}$$

Using the arm motion obtained from equation (11), the internal forces and moments acting on the sprung mass can be determined from equations (4) to (5).

2.1.3 *Vehicle body dynamic model*

The vehicle body dynamic model determines the dynamic behaviour of the sprung mass using the internal forces and moments obtained from the arm dynamic model. The dynamic equations of the sprung mass can

be obtained from the d'Alembert principle as follows

$$\sum_{i=1}^{6} F_{sxi} = m_s\left[\dot{v}_x + v_z\left(\dot{\theta} - v_y\right)\dot{\varphi}\right]$$

$$\sum_{i=1}^{6} F_{syi} = m_s\left[\dot{v}_y + v_x(\dot{\varphi} - v_z)\dot{\phi}\right]$$

$$\sum_{i=1}^{6} F_{szi} = m_s\left[\dot{v}_z + v_y\left(\dot{\phi} - v_x\right)\dot{\theta}\right] \tag{12}$$

$$\sum_{i=1}^{6} M_{sxi} + t_w\left\{\sum_{i=1}^{3} F_{sz(2i-1)} - \sum_{i=1}^{3} F_{tz(2i)}\right\} = I_x\ddot{\phi} + (I_z - I_y)\dot{\theta}\dot{\varphi}$$

$$\sum_{i=1}^{6} T_{S\&D\_i} + \left\{-l_f\sum_{i=1}^{2} F_{szi} - l_m\sum_{i=3}^{4} F_{szi} + l_r\sum_{i=5}^{6} F_{szi}\right\} = I_y\ddot{\theta} + (I_x - I_z)\dot{\varphi}\dot{\phi}$$

$$\sum_{i=1}^{6} M_{szi} + t_w\sum_{i=1}^{3}\left(F_{sx(2i)} - F_{sx(2i-1)}\right) + \left\{l_f\sum_{i=1}^{2} F_{syi} + l_m\sum_{i=3}^{4} F_{syi} - l_r\sum_{i=5}^{6} F_{syi}\right\} = I_z\ddot{\varphi} + (I_y - I_x)\dot{\phi}\dot{\theta} \tag{13}$$

2.2 Validation of dynamic model

Validation of the vehicle dynamic model has been conducted by comparing simulation results to the test data of the RVAS. For the validation of the dynamic model, the driving control algorithm which was implemented in the vehicle test is used identically in the dynamic model simulation. Also, the desired speed obtained from the vehicle test is used in the simulation. Figure 6 shows a comparison of test data and simulation results. From Fig. 6, it is found that the simulation results are almost identical to the test data except for the yaw rate, as shown in Fig. 6(b). The difference between the test data and the simulation results is due to the vertical road profile and an offset of the mass centre of the test platform. In the case of the vehicle test, the yaw rate is fluctuated by the road profile. Also, the offset of the mass centre causes a smaller left yaw motion than the right yaw motion in an identical yaw motion command. However, the simulation results agree generally with the test data, suggesting that the designed dynamic model is feasible as a test platform for development of the driving controller.

3 CONTROLLER DESIGN

In this section, the driving control algorithm based on skid steering is designed to control vehicle motion according to the control mode. There are two control modes. One is the remote control manoeuvring mode. In the case of the remote control manoeuvring mode, the vehicle motion is controlled according to the remote driver's command, desired speed, and steering command. The other is the autonomous driving control mode for tracking the desired trajectory. The control mode is determined by the remote driver. Figure 7 shows a control strategy for the driving controller proposed in this study. Since it is difficult to determine the wheel torque command directly, the driving control algorithm for the RVAS is designed with four parts as follows: a speed controller which determines a total traction force for following a desired speed; a lateral motion controller which computes a yaw moment input to track a desired yaw rate or a desired trajectory according to the control mode; a tyre force distribution algorithm that calculates an optimal desired longitudinal tyre force at each wheel; and a wheel torque controller that determines the wheel torque command at each wheel.

A schematic diagram of the proposed driving control algorithm is shown in Fig. 8. The speed controller in the upper-level control is designed to follow the desired speed using the PI control method [**8**, **14**, **15**]. The lateral motion controller determines the yaw moment input in order to track the desired yaw motion which is determined according to the control mode, the remote control mode, and the autonomous driving control mode. The upper-level control inputs, the total traction force, and the yaw moment input should be applied to the RVAS using the longitudinal tyre force distribution algorithm and wheel torque control. Therefore, the objective of the tyre force distribution algorithm is to determine how much force is required at each wheel. From the concept of the friction circle, the desired longitudinal tyre force of each wheel is determined in proportion to the vertical tyre force of each wheel. Finally, a wheel torque controller is designed to track the desired longitudinal tyre force and at the same time keep the wheel slip ratio of each wheel below a limit value. Additionally, longitudinal and vertical tyre forces are estimated for optimal tyre force distribution and wheel slip control [**14**, **16**–**18**].

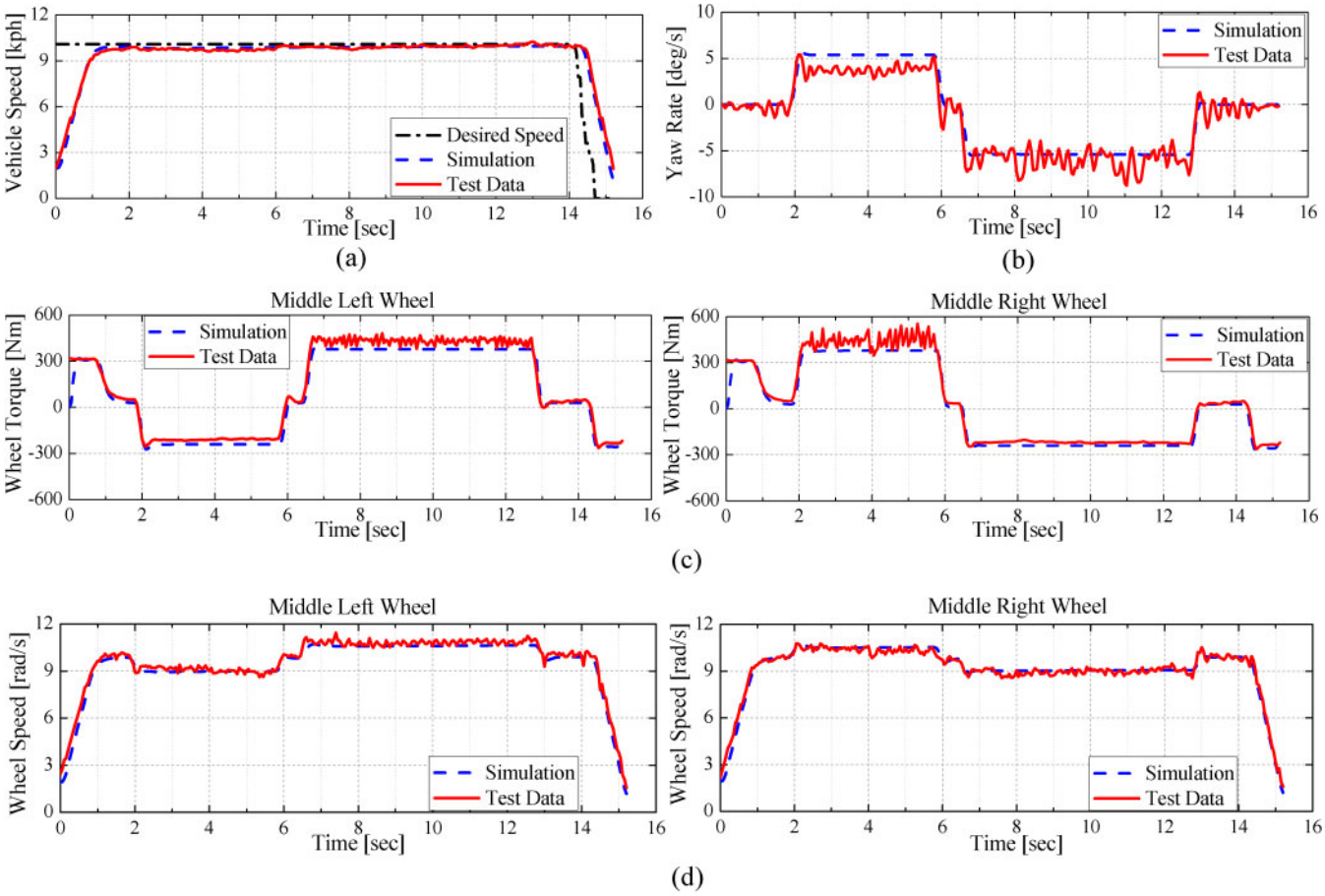

Fig. 6 Comparison of test data and simulation results: (a) vehicle speed (km/h), (b) yaw rate (deg/s), (c) wheel torque input (middle wheel) (N m), and (d) wheel speed (middle wheel) (rad/s)

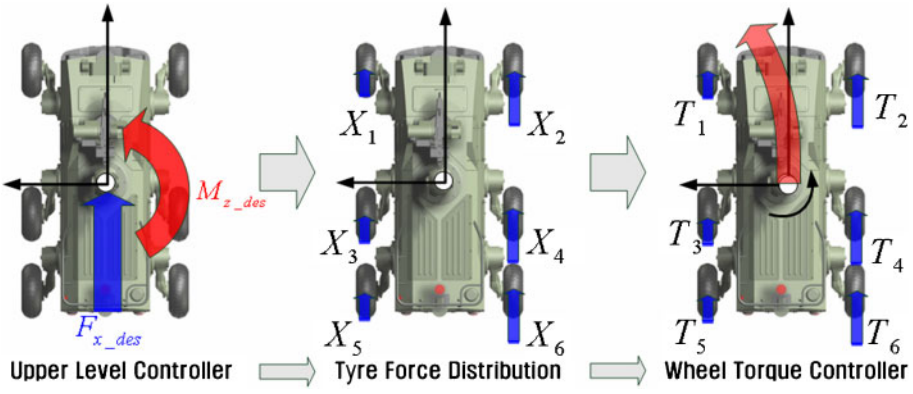

Fig. 7 Control strategy of the driving controller based on a skid steering

3.1 Upper-level control

The upper-level control consists of the speed controller and the lateral motion controller, as shown in Fig. 9. In the upper-level control, the speed controller computes a total traction force, F_{x_des}, for following a desired speed. In this paper, the speed controller is designed based on the PI control method. Also, the lateral motion controller determines yaw moment input, M_{z_des}, according to the control mode. The control mode is selected by remote driver input, and there exist two control modes: the remote control manoeuvring mode and the autonomous driving control mode. In the case of the remote control mode, the yaw rate controller is activated and computes the yaw moment input for following the desired yaw rate. In the remote control manoeuvring

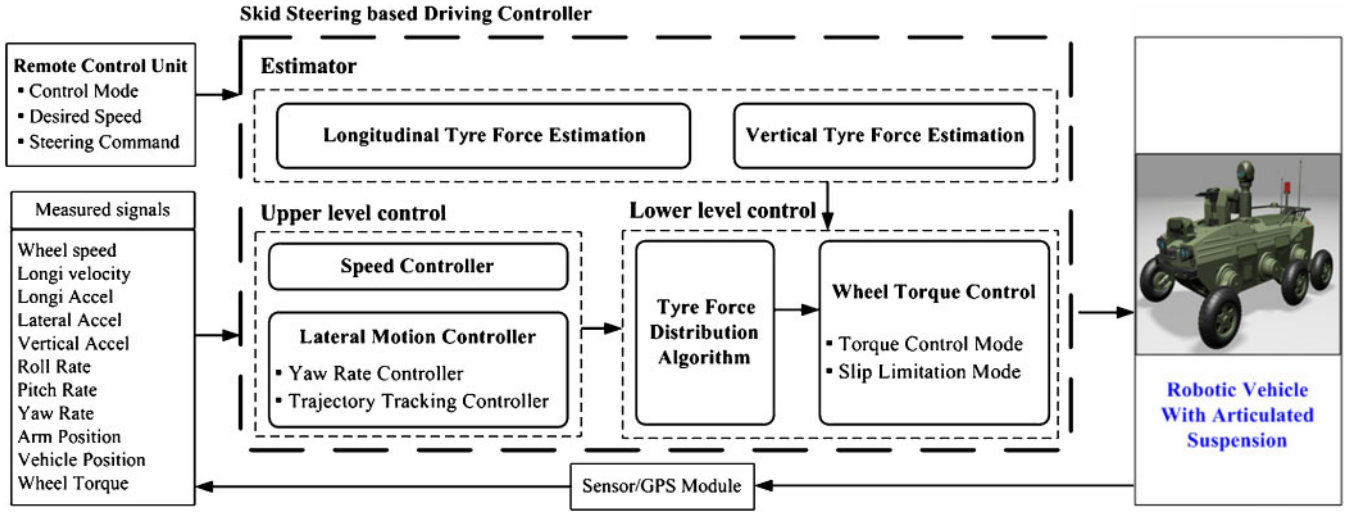

Fig. 8 Block diagram of autonomous driving control algorithm based on a skid steering

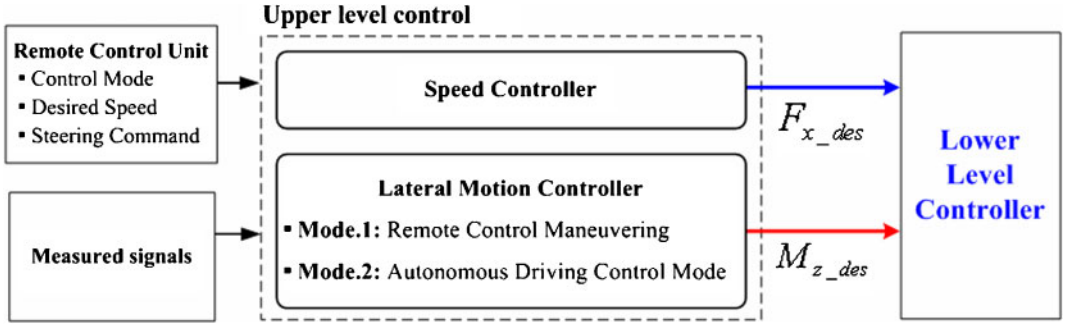

Fig. 9 Upper-level control

mode, a desired yaw rate is generated based on the remote driver's steering command. In the autonomous driving control mode, the trajectory tracking controller is activated and determines the yaw moment input to track the prescribed trajectory. The upper-level control inputs are applied to the test platform through the lower level-controller.

3.1.1 *Remote control manoeuvring*

In the remote control mode, the yaw rate controller is activated in order to force the vehicle to track a desired yaw rate generated by a remote driver's steering command, δ_{com}. The yaw rate controller determines the yaw moment input to reduce the yaw rate error between the desired and the actual yaw rates. The desired yaw rate, γ_{d}, is determined using the remote driver's steering command and the first-order transfer function as [**4**]

$$\gamma_{\text{d}} = \frac{\gamma_{\text{ss}}}{1+\tau_{\text{SR}}s}\delta_{\text{com}} \tag{14}$$

where τ_{SR} denotes the time constant and γ_{ss} can be calculated based on a 2DOF bicycle model as

$$\gamma_{\text{ss}} = \frac{2\cdot v_x\{C_{\text{f}}C_{\text{m}}(l_{\text{wf}}+l_{\text{wm}})+C_{\text{f}}C_{\text{r}}(l_{\text{wf}}+l_{\text{wr}})\}}{2\left\{C_{\text{f}}C_{\text{m}}(l_{\text{wf}}+l_{\text{wm}})^2+C_{\text{f}}C_{\text{r}}(l_{\text{wf}}+l_{\text{wr}})^2+C_{\text{m}}C_{\text{r}}(l_{\text{wm}}-l_{\text{wr}})^2\right\}-2mv_x^2(l_{\text{wf}}C_{\text{f}}-l_{\text{wm}}C_{\text{m}}-l_{\text{wr}}C_{\text{r}})} \tag{15}$$

A 2DOF bicycle model modified as a skid-steering vehicle is used to design the yaw rate controller, as shown in Fig. 10. Equation (16) represents the dynamic equation of the modified bicycle model

$$\begin{aligned} m(\dot{v}_y+v_x\dot{\varphi}) &= 2F_{\text{yf}}+2F_{\text{ym}}+2F_{\text{yr}} \\ I_z\ddot{\varphi} &= l_{\text{wf}}F_{\text{yf}}-l_{\text{wm}}F_{\text{ym}}-l_{\text{wr}}F_{\text{yr}}+M_{z\_\text{des}} \end{aligned} \tag{16}$$

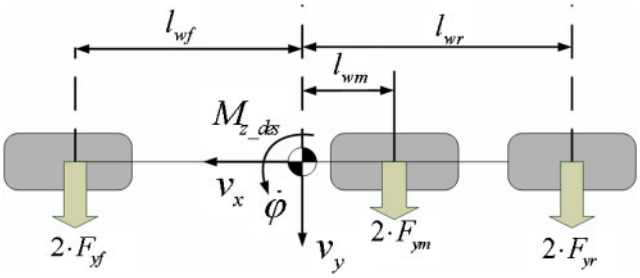

Fig. 10 Modified 2DOF bicycle model

The sliding mode control method is used for the design of the yaw rate controller, and the sliding surface is defined using the difference between the desired yaw rate and the actual yaw rate as follows

$$s = \dot{\varphi} - \gamma_{\mathrm{d}} \tag{17}$$

The control objective is to keep the sliding surface at zero. This can be achieved by choosing the control law such that

$$\frac{1}{2}\frac{\mathrm{d}}{\mathrm{d}t}s^2 = s\dot{s} < -\eta|s| \leqslant -K|s| \tag{18}$$

where K denotes the control gain. Using equations (16) to (18), the yaw moment input for tracking the desired yaw rate can be obtained as

$$M_{z\_\mathrm{des}} = -\left\{2l_{\mathrm{wf}}F_{\mathrm{yf}} - 2l_{\mathrm{wm}}F_{\mathrm{ym}} - 2l_{\mathrm{wr}}F_{\mathrm{yr}}\right\} - I_z K\,\mathrm{sgn}(s) \tag{19}$$

In equation (19), the lateral tyre forces can be expressed using the linear tyre model as

$$\begin{aligned} F_{\mathrm{yf}} &= C_{\mathrm{f}}\left(-\frac{v_y + l_{\mathrm{wf}}\dot{\varphi}}{v_x}\right) \\ F_{\mathrm{ym}} &= C_{\mathrm{m}}\left(-\frac{v_y - l_{\mathrm{wm}}\dot{\varphi}}{v_x}\right) \\ F_{\mathrm{yr}} &= C_{\mathrm{m}}\left(-\frac{v_y - l_{\mathrm{wr}}\dot{\varphi}}{v_x}\right) \end{aligned} \tag{20}$$

Substituting equation (20) into equation (19), the yaw moment input can be obtained as

$$M_{z\_\mathrm{des}} = -A_3 I_z \beta - \frac{A_4}{v_x} I_z \gamma - I_z K\,\mathrm{sgn}(s) \tag{21}$$

where

$$\begin{aligned} A_3 &= -\frac{2(l_{\mathrm{f}}C_{\mathrm{f}} - l_{\mathrm{m}}C_{\mathrm{m}} - l_{\mathrm{r}}C_{\mathrm{r}})}{I_z} \\ A_4 &= -\frac{2\left(l_{\mathrm{f}}^2 C_{\mathrm{f}} + l_{\mathrm{m}}^2 C_{\mathrm{m}} + l_{\mathrm{r}}^2 C_{\mathrm{r}}\right)}{I_z} \end{aligned}$$

Finally, the saturation function with boundary, Φ, is used to cope with the chattering phenomenon as

$$M_{z\_\mathrm{des}} = \begin{cases} -A_3 I_z \beta - \dfrac{A_4}{v_x} I_z \gamma - I_z K\,\mathrm{sgn}\left(\dfrac{s}{\Phi}\right) & \text{if } (|s| \geq \Phi) \\ -A_3 I_z \beta - \dfrac{A_4}{v_x} I_z \gamma - I_z K \dfrac{s}{\Phi} & \text{if } (|s| < \Phi) \end{cases} \tag{22}$$

The control parameters for the yaw rate controller are shown in Table 2.

3.1.2 *Autonomous driving control*

The trajectory tracking controller is activated in the autonomous driving control mode. The controller computes the yaw moment input in order to track the desired trajectory. In this study, the trajectory tracking controller is designed based on the optimal finite preview control method, as shown in Fig. 11 [**8**, **9**].

In Fig. 11, lateral position error, y_r, is defined as the lateral distance between the vehicle c.g. (C) and the centre-line of the desired trajectory (R). Yaw angle error, $\varphi - \varphi_{\mathrm{d}}$, is defined using the yaw angle of the vehicle and the desired yaw angle as dictated by the desired trajectory. The rate of change of lateral position error and yaw angle error are defined as follows

$$\begin{aligned} \Delta y_{\mathrm{r}} &= v_y \Delta t + v_x \Delta t(\varphi - \varphi_{\mathrm{d}}) \\ \dot{y}_{\mathrm{r}} &= v_y + v_x(\varphi - \varphi_{\mathrm{d}}) \end{aligned} \tag{23}$$

$$\Delta\varphi_{\mathrm{d}} = \frac{v_x \Delta t}{\rho} \Rightarrow \dot{\varphi}_{\mathrm{d}} = \frac{v_x}{\rho} \tag{24}$$

where ρ denotes the curvature radius of the desired trajectory.

The trajectory tracking controller is designed to eliminate the lateral position error and the yaw angle error through a combination of feedback and feedforward control. The feedback control input of the trajectory tracking controller is computed using the lateral position error and the yaw angle error.

Table 2 Control parameters for yaw rate controller

Symbol	Value	Symbol	Value
τ_{SR}	0.01 s	C_{f}	22 031 N/rad
K	2.8	C_{m}	24 274 N/rad
Φ	5.0 deg/s	C_{r}	20 790 N/rad

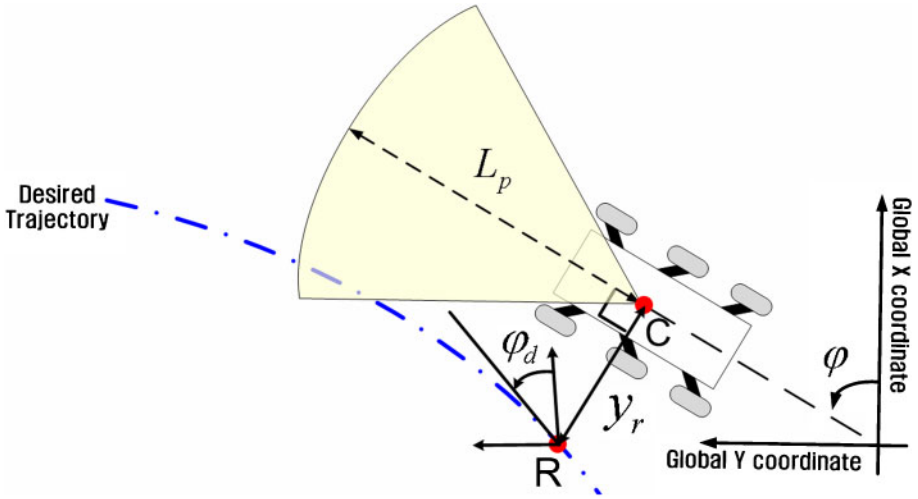

Fig. 11 Trajectory tracking controller based on an optimal finite preview control

The feedforward control input is determined using the road information within the preview distance. To develop the trajectory tracking controller based on the optimal finite preview control theory, preview distance, L_p, is transformed into preview time, T_p, as

$$T_p = \frac{L_p}{v_x} \tag{25}$$

A modified 2DOF bicycle model described in the previous section is used similarly to design the trajectory tracking controller. Using the linear tyre model of equation (20) and equations (23) and (24), the lateral tyre forces can be represented as

$$\begin{aligned}
F_{yf} &= C_f\left\{-\frac{\dot{y}_r + l_{wf}(\dot{\varphi}-\dot{\varphi}_d)}{v_x} + (\varphi-\varphi_d) - \frac{l_{wf}}{v_x}\dot{\varphi}_d\right\}\\
F_{yr} &= C_r\left\{-\frac{\dot{y}_r - l_{wr}(\dot{\varphi}-\dot{\varphi}_d)}{v_x} + (\varphi-\varphi_d) + \frac{l_{wr}}{v_x}\dot{\varphi}_d\right\}\\
F_{ym} &= C_m\left\{-\frac{\dot{y}_r - l_{wm}(\dot{\varphi}-\dot{\varphi}_d)}{v_x} + (\varphi-\varphi_d) + \frac{l_{wm}}{v_x}\dot{\varphi}_d\right\}
\end{aligned} \tag{26}$$

Substituting equation (26) into equation (16), the state equations for the design of the trajectory tracking controller can be obtained as

$$\begin{aligned}
\dot{x} &= Ax + BM_{z_des} + F_d w_d\\
x &= [\,y_r \quad \dot{y}_r \quad \varphi-\varphi_d \quad \dot{\varphi}-\dot{\varphi}_d\,]^T
\end{aligned} \tag{27}$$

where

$$A = \begin{bmatrix} 0 & 1 & 0 & 0\\ 0 & \frac{A_1}{v_x} & -A_1 & \frac{A_2}{v_x}\\ 0 & 0 & 0 & 1\\ 0 & \frac{A_3}{v_x} & -A_3 & \frac{A_4}{v_x} \end{bmatrix}$$

$$B = \begin{bmatrix} 0\\ 0\\ 0\\ \frac{1}{I_z} \end{bmatrix}, \quad F_d = \begin{bmatrix} 0 & 0\\ 1 & 0\\ 0 & 0\\ 0 & 1 \end{bmatrix}$$

$$w_d = \begin{bmatrix} -v_x\dot{\varphi}_d + \frac{A_2}{v_x}\dot{\varphi}_d\\ \frac{A_4}{v_x}\dot{\varphi}_d - \ddot{\varphi}_d \end{bmatrix}$$

$$A_1 = -\frac{2(C_f + C_m + C_r)}{m}$$

$$A_2 = -\frac{2(l_{wf}C_f - l_{wm}C_m - l_{wr}C_r)}{m}$$

$$A_3 = -\frac{2(l_{wf}C_f - l_{wm}C_m - l_{wr}C_r)}{I_z}$$

$$A_4 = -\frac{2(l_{wf}^2C_f + l_{wm}^2C_m + l_{wr}^2C_r)}{I_z}$$

In this study, the yaw moment input is determined using the optimal finite preview control method. The yaw moment input consists of a feedback control input, $-K_{opt}x(t)$, and a feedforward control input, $M_{pre}(t)$, as in equation (28)

$$M_{z\_des}(t) = -K_{opt}x(t) + M_{pre}(t) \tag{28}$$

The feedback gain in equation (28) can be obtained using the control algebraic Riccati equation and the feedforward input can be computed based on the finite preview control method as in equation (29) [**8**, **9**]

$$M_{\text{pre}}(t) = -R^{-1}B^{\text{T}}\left[\int_0^{\text{T}_p} e^{A_c^{\text{T}}\tau}P_{\text{ss}}F_{\text{d}}w(t+\tau)\,\text{d}\tau - \left(A_{\text{c}}^{\text{T}}\right)^{-1}e^{A_c^{\text{T}}\text{T}_{\text{p}}}P_{\text{ss}}F_{\text{d}}w_{\text{d}}\left(t+T_{\text{p}}\right)\right] \quad (29)$$

where $A_{\text{c}} = A - BR^{-1}B^{\text{T}}P_{\text{ss}}$ and P_{ss} denotes the solution of the control algebraic Riccati equation. From equation (29), it is clear that the yaw moment input is computed using the desired trajectory information between t and $t+T_{\text{p}}$.

Equation (29) indicates that an integral operation with respect to τ has to be performed at each time in order to determine the yaw moment input. In order to implement the optimal finite preview control easily, the integration can be replaced by a finite summation of the form as

$$M_{\text{pre}}(t) = -R^{-1}B^{\text{T}}\left\{\sum_{i=0}^{N_{\text{total}}} e^{A_c^{\text{T}}(\Delta\text{T}i)}P_{\text{ss}}F_{\text{d}}w(t+\Delta Ti)\Delta T - \left(A_{\text{c}}^{\text{T}}\right)^{-1}e^{A_c^{\text{T}}\text{T}_{\text{p}}}P_{\text{ss}}F_{\text{d}}w_{\text{d}}\left(t+T_{\text{p}}\right)\right\} \quad (30)$$

where $N_{\text{total}}\Delta T = T_{\text{p}}$ and ΔT is sufficiently small. The control parameters for the trajectory tracking controller are shown in Table 3.

Table 3 Control parameters for trajectory tracking controller

Symbol	Value	Symbol	Value
T_{p}	0.65 s	N_{total}	20

3.2 Lower-level controller

A lower-level controller is designed to apply the upper-level control inputs to the test platform. The lower-level controller consists of the tyre force distribution algorithm and the wheel torque controller, as shown in Fig. 12. In tyre force distribution, the desired longitudinal tyre force of each wheel, X_i, is computed using the estimated vertical tyre force, $\hat{F}_{tzi}$ [**14**, **16**, **17**]. The wheel torque controller determines wheel torque command, $T_{\text{com\_}i}$, at each wheel using the desired longitudinal tyre force and estimated longitudinal tyre force, $\hat{F}_{txi}$, in order to keep the slip ratio at each wheel below a limit value as well as to track the desired longitudinal tyre force.

3.2.1 *Tyre force distribution algorithm*

In section 3.1, the total traction force input and the yaw moment input are determined. These upper-level control inputs to the test platform should occur through the tyre force distribution. Therefore, the objective of the tyre force distribution algorithm is to compute how much force should be generated at each wheel. From the concept of friction circle (where the tyre force magnitude acting on a tyre is

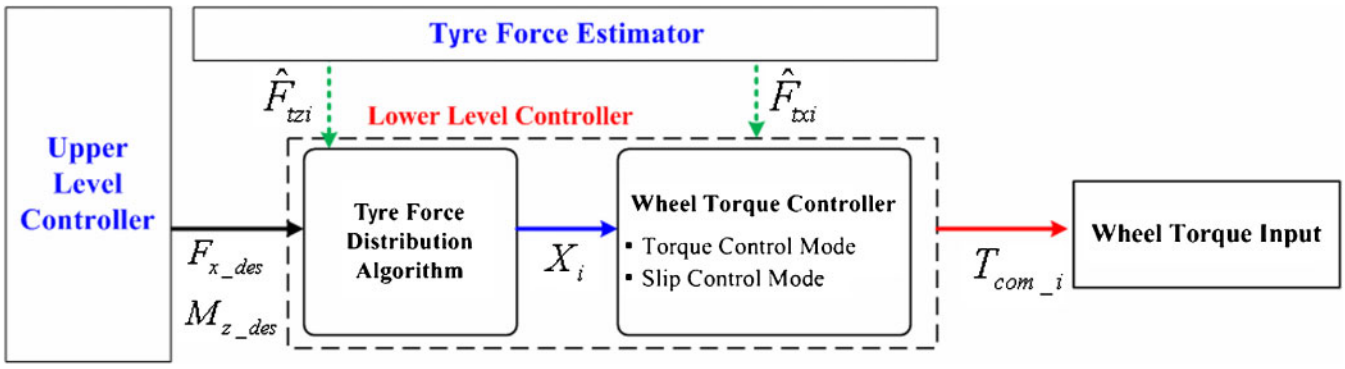

Fig. 12 Lower-level controller

proportional to the vertical tyre force), it is well known that the tyre force magnitude acting on a tyre is proportional to the vertical tyre force. Using this concept and to simplify the optimization problem as well as to obtain a linear equation system, the cost function as equation (31) is chosen in order to obtain the desired longitudinal tyre force at each wheel [**19**]

$$J_{\cos t} = \sum_{i=1}^{6} \left(W_i \frac{X_i^2}{\hat{F}_{tzi}^2} \right) \tag{31}$$

where W_i denotes the weighting coefficient at the ith wheel.

The desired tyre forces have to satisfy the following constraints as equations (32) and (33) in order to apply the total traction force and the yaw moment input to the test platform

$$F_{x\_des} = X_1 + X_2 + X_3 + X_4 + X_5 + X_6 \tag{32}$$

$$M_{z\_des} = -t_w[(X_1 - X_2) + (X_3 - X_4) + (X_5 - X_6)] \tag{33}$$

Substituting equations (32) and (33) into equation (31), the cost function of equation (31) is not subjected to any constraints, and its optimum can be determined as shown in equation (34)

$$\begin{aligned}
\frac{\partial J_{\text{cost}}}{\partial X_1} &= 0 = \frac{2W_1}{\hat{F}_{tz1}} X_1 - \frac{2W_5}{\hat{F}_{tz5}} \left[\frac{F_{x_des}}{2} - \frac{M_{z_des}}{2t_w} - X_1 - X_3 \right], \\
\frac{\partial J_{\text{cost}}}{\partial X_2} &= 0 = \frac{2W_2}{\hat{F}_{tz2}} X_2 - \frac{2W_6}{\hat{F}_{tz6}} \left[\frac{F_{x_des}}{2} + \frac{M_{z_des}}{2t_w} - X_2 - X_4 \right], \\
\frac{\partial J_{\text{cost}}}{\partial X_3} &= 0 = \frac{2W_3}{\hat{F}_{tz3}} X_3 - \frac{2W_5}{\hat{F}_{tz5}} \left[\frac{F_{x_des}}{2} - \frac{M_{z_des}}{2t_w} - X_1 - X_3 \right], \\
\frac{\partial J_{\text{cost}}}{\partial X_4} &= 0 = \frac{2W_4}{\hat{F}_{tz4}} X_4 - \frac{2W_6}{\hat{F}_{tz6}} \left[\frac{F_{x_des}}{2} + \frac{M_{z_des}}{2t_w} - X_2 - X_4 \right]
\end{aligned} \tag{34}$$

As a result, the desired longitudinal tyre force at each wheel can be obtained based on the estimated vertical tyre force and upper-level control inputs as

$$\begin{bmatrix} X_1 \\ X_2 \\ X_3 \\ X_4 \end{bmatrix} = \begin{bmatrix} \frac{W_1}{\hat{F}_{tz1}^2} + \frac{W_5}{\hat{F}_{tz5}^2} & 0 & \frac{W_5}{\hat{F}_{tz5}^2} & 0 \\ 0 & \frac{W_2}{\hat{F}_{tz2}^2} + \frac{W_6}{\hat{F}_{tz6}^2} & 0 & \frac{W_6}{\hat{F}_{tz6}^2} \\ \frac{W_5}{\hat{F}_{tz5}^2} & 0 & \frac{W_3}{\hat{F}_{tz3}^2} + \frac{W_5}{\hat{F}_{tz5}^2} & 0 \\ 0 & \frac{W_6}{\hat{F}_{tz6}^2} & 0 & \frac{W_4}{\hat{F}_{tz4}^2} + \frac{W_6}{\hat{F}_{tz6}^2} \end{bmatrix}^{-1} \begin{bmatrix} \frac{W_5}{\hat{F}_{tz5}^2} \left\{ \frac{F_{x\_des}}{2} - \frac{M_{z\_des}}{2t_w} \right\} \\ \frac{W_6}{\hat{F}_{tz6}^2} \left\{ \frac{F_{x\_des}}{2} + \frac{M_{z\_des}}{2t_w} \right\} \\ \frac{W_5}{\hat{F}_{tz5}^2} \left\{ \frac{F_{x\_des}}{2} - \frac{M_{z\_des}}{2t_w} \right\} \\ \frac{W_6}{\hat{F}_{tz6}^2} \left\{ \frac{F_{x\_des}}{2} + \frac{M_{z\_des}}{2t_w} \right\} \end{bmatrix}, \quad \begin{aligned} X_5 &= \frac{F_{x\_des}}{2} - \frac{M_{z\_des}}{2t_w} - X_1 - X_3 \\ X_6 &= \frac{F_{x\_des}}{2} + \frac{M_{z\_des}}{2t_w} - X_2 - X_4 \end{aligned} \tag{35}$$

3.2.2 *Wheel torque controller*

The wheel torque controller is designed to determine the wheel torque input at each wheel in order to generate vehicle motion. The aim of the RVAS is to drive on various rough terrains. Also, it is difficult to obtain the complete characteristics of the longitudinal tyre force according to driving conditions. Therefore, it is assumed that a characteristic of longitudinal tyre force is unknown in designing the wheel torque controller [**14**].

The wheel torque controller is designed to keep a wheel slip ratio of each wheel below a limit value, $\lambda_{\max}$, as well as to track the desired longitudinal tyre force. In the case of a sufficiently small slip ratio, the wheel torque command can be determined as equation (36) in order to track the desired longitudinal tyre force

$$T_{\text{com}\_i}(k) = R_i X_i(k) \tag{36}$$

However, the above control input may cause deviation of the wheel slip ratio when the wheel is lifted off or excessive longitudinal tyre force is required. In this study, when the wheel slip ratio is larger than the limit value, the wheel torque controller is designed so that the actual wheel speed tracks the desired wheel speed for slip control. The desired wheel speed is represented as [**20**]

$$\omega_{i\_\text{des}} = \begin{cases} \dfrac{v_{txi}}{R_i(1-\lambda_{\max})} & \text{if } (\lambda > \lambda_{\max}) \\ \dfrac{v_{txi}}{R_i}(1-\lambda_{\max}) & \text{if } (\lambda < -\lambda_{\max}) \end{cases} \tag{37}$$

Table 4 Control parameters for wheel torque controller

Symbol	Value	Symbol	Value
K_w	80.0	λ_{max}	0.2
Φ_w	5.0 rad/s		

where v_{txi} denotes the longitudinal velocity at the tyre centre. The wheel torque command for tracking the desired wheel speed is computed based on the sliding mode control method and wheel dynamics as follows

$$s_w = \omega_{i\_des}(k) - \omega_i(k), \quad \frac{1}{2}\frac{d}{dt}s_w^2 = s_w\dot{s}_w = -K_w|s_w|$$
$$\dot{s}_w = -\dot{\omega}_i = -\frac{1}{J_w}\left\{T_{com\_i}(k) - R_i\hat{F}_{txi}(k)\right\} = -K_w\,\mathrm{sgn}(s_w) \tag{38}$$

where K_w is a positive constant. As a result, the wheel torque command can be determined as shown in equation (39)

$$T_{com\_i}(k) = \begin{cases} R_iX_i(k) & \text{if } (|\lambda| < \lambda_{max}) \\ R_i\hat{F}_{txi}(k) + J_wK_w sat(s_w/\Phi_w) & \text{if } (|\lambda| \geqslant \lambda_{max}) \end{cases} \tag{39}$$

where Φ_w denotes the boundary condition of the saturation function. Table 4 shows the control parameters for the wheel torque controller.

4 TYRE FORCE ESTIMATION

As mentioned in section 3, the estimated longitudinal and vertical tyre forces are required for the optimal tyre force distribution and the wheel slip control in the lower-level control. Figure 13 shows the schematic diagram of the tyre force estimation. The angular acceleration at each wheel, $\hat{\dot{\omega}}_i(k)$, can be estimated using the measured wheel speed. Also, the estimated longitudinal tyre force, $\hat{F}_{txi}(k)$, can be calculated using $\hat{\dot{\omega}}_i(k)$ and the wheel torque measured earlier, $T_i(k-1)$, based on wheel dynamics. Finally, vertical tyre force at each wheel can be obtained using arm dynamics.

4.1 Longitudinal tyre force estimation

A longitudinal tyre force can be estimated using the estimated wheel angular acceleration and the wheel dynamic equation. The state equation for estimation of wheel angular acceleration is obtained from the Taylor formula of wheel speed as follows [**21**]

$$\omega_i(t+\Delta T) = \omega_i(t) + \Delta T\dot{\omega}_i(t) + \frac{\Delta T^2}{2}\ddot{\omega}_i(t) + d_1$$
$$\dot{\omega}_i(t+\Delta T) = \dot{\omega}_i(t) + \Delta T\ddot{\omega}_i(t) + d_2$$
$$\ddot{\omega}_i(t+\Delta T) = \ddot{\omega}_i(t) + d_3 \tag{40}$$

where ΔT is the sampling period and d_i denotes disturbance. In equation (40), the wheel angular speed can be measured; that is

$$y(t) = [\,1 \quad 0 \quad 0\,][\,\omega_i(t) \quad \dot{\omega}_i(t) \quad \ddot{\omega}_i(t)\,]^T \tag{41}$$

The state equation can be expressed by discretization of equations (40) and (41) as

$$x(k+1) = \overbrace{\begin{bmatrix} 1 & \Delta T & \Delta T^2/2 \\ 0 & 1 & \Delta T \\ 0 & 0 & 1 \end{bmatrix}}^{A_{esti}} \begin{bmatrix} \omega_i(k) \\ \dot{\omega}_i(k) \\ \ddot{\omega}_i(k) \end{bmatrix} + \overbrace{\begin{bmatrix} 1 & 0 & 0 \\ 0 & 1 & 0 \\ 0 & 0 & 1 \end{bmatrix}}^{G_{esti}} \begin{bmatrix} d_1 \\ d_2 \\ d_3 \end{bmatrix}$$
$$y(k) = \overbrace{[\,1 \quad 0 \quad 0\,]}^{H_{esti}} x(k) + v(k) \tag{42}$$

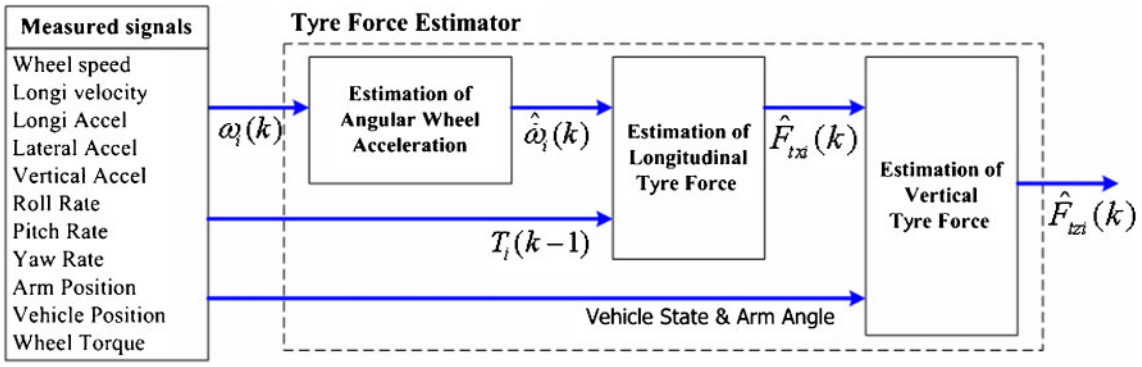

Fig. 13 Tyre force estimation

where $v(k)$ is measurement noise. Suppose that $d_i(k)$ and $v(k)$ are zero-mean white noise separately, whose covariance values are $Q_{\text{esti}}(k)$ and $R_{\text{esti}}(k)$ as

$$Q_{\text{esti}}(k)=\begin{bmatrix}0&0&0\\0&0&0\\0&0&q\end{bmatrix},\quad R_{\text{esti}}(k)=r \tag{43}$$

Using the Kalman filter method and equations (42) and (43), the estimated wheel acceleration can be obtained as follows

$$\begin{aligned}\hat{x}(k|k)&=A_{\text{esti}}\hat{x}(k-1|k-1)\\&\quad+L(k)\{y(k)-H_{\text{esti}}A_{\text{esti}}\hat{x}(k-1|k-1)\}\end{aligned} \tag{44}$$

where $L(k)$ denotes the Kalman filter gain. As a result, $\hat{F}_{\text{tx}i}(k)$ can be calculated using the wheel torque measured earlier, $T_i(k-1)$, and the estimated wheel acceleration, $\hat{\dot{\omega}}_i(k|k)$, based on wheel dynamics as

$$\hat{F}_{\text{tx}i}(k)=\frac{1}{R_i}\left\{T_i(k-1)-\frac{1}{J_{\text{w}}}\hat{\dot{\omega}}_i(k|k)\right\} \tag{45}$$

4.2 Vertical tyre force estimation

The vertical tyre force can be estimated approximately based on the steady state arm dynamics, as shown in Fig. 14 and equation (46)

$$\begin{aligned}\sum M_y&=-\Delta T_{\text{S\&D\_}i}+l_{\text{arm}}\sin\theta_{\text{arm\_}i}\Delta\hat{F}_{\text{tz}i}\\&\quad-l_{\text{arm}}\cos\theta_{\text{arm\_}i}\hat{F}_{\text{tx}i}\\&=-\left(m_{\text{w}}\ddot{x}_{\text{w\_}i}+\frac{m_{\text{arm}}}{2}\ddot{x}_{\text{arm\_}i}\right)l_{\text{arm}}\cos\theta_{\text{arm\_}i}\\&\quad+\left(m_{\text{w}}\ddot{z}_{\text{w\_}i}+\frac{m_{\text{arm}}}{2}\ddot{z}_{\text{arm\_}i}\right)l_{\text{arm}}\sin\theta_{\text{arm\_}i}=0\end{aligned} \tag{46}$$

where $\Delta T_{\text{S\&D\_}i}$ denotes the variation of the spring and damping torques at the ith arm rod as

$$\begin{aligned}\Delta T_{\text{S\&D\_}i}&=k_{\text{s}}\Delta\theta_{\text{arm\_}i}+c_{\text{d}}\Delta\dot{\theta}_{\text{arm\_}i}\\\Delta\theta_{\text{arm\_}i}&=\theta_{\text{arm\_}i}-\theta_{\text{arm\_static}}\end{aligned} \tag{47}$$

In equation (46), $\ddot{x}_{\text{w\_}i}$, $\ddot{z}_{\text{w\_}i}$, $\ddot{x}_{\text{arm\_}i}$, and $\ddot{z}_{\text{arm\_}i}$ can be expressed approximately as

$$\begin{aligned}\ddot{r}_{\text{w}i}&=[\,\ddot{x}_{\text{w}i}\quad\ddot{y}_{\text{w}i}\quad\ddot{z}_{\text{w}i}\,]^{\text{T}}\\&=\ddot{r}_{\text{cg}}+\omega_{\text{arm\_}i}\times\omega_{\text{arm\_}i}\times r_{\text{w}i/\text{cg}}+\alpha/_{\text{cg}}\times r_{\text{w/cg}}\\\ddot{r}_{\text{arm\_}i}&=[\,\ddot{x}_{\text{arm\_}i}\quad\ddot{y}_{\text{arm\_}i}\quad\ddot{z}_{\text{arm\_}i}\,]^{\text{T}}\\&=\ddot{r}_{\text{cg}}+\omega_{\text{arm\_}i}\times\omega_{\text{arm\_}i}\times r_{\text{arm\_}i/\text{cg}}+\alpha/_{\text{cg}}\times r_{\text{arm\_}i/\text{cg}}\end{aligned} \tag{48}$$

where $r_{\text{w}i/\text{cg}}$ denotes the distance vector from c.g. to the ith wheel, $r_{\text{arm\_}i/\text{cg}}$ the distance vector from c.g. to the mass centre of the ith arm rod respectively. $r_{\text{w}i/\text{cg}}$ and $r_{\text{arm\_}i/\text{cg}}$ can be obtained as

$$\begin{aligned}r_{\text{w}i/\text{cg}}&=[l_i-l_{\text{arm}}\sin(\theta_{\text{arm\_}i})\pm t_{\text{w}}-l_{\text{arm}}\cos(\theta_{\text{arm\_}i})]^{\text{T}}\\r_{\text{arm\_}i/\text{cg}}&=\left[l_i-\frac{l_{\text{arm}}}{2}\sin(\theta_{\text{arm\_}i})\pm t_{\text{w}}-\frac{l_{\text{arm}}}{2}\cos(\theta_{\text{arm\_}i})\right]^{\text{T}}\end{aligned} \tag{49}$$

Substituting equation (48) into equation (46), the variation of the vertical tyre force at the ith wheel can be obtained as

$$\begin{aligned}\Delta\hat{F}_{\text{tz}i}&=\frac{k_{\text{s}}\Delta\theta_{\text{arm\_}i}+c_{\text{d}}\Delta\dot{\theta}_{\text{arm\_}i}}{l_{\text{arm}}\sin\theta_{\text{arm\_}i}}+\frac{\hat{F}_{\text{tx}i}}{\tan\theta_{\text{arm\_}i}}-\frac{\left(m_{\text{w}}+\frac{m_{\text{arm}}}{2}\right)}{\tan\theta_{\text{arm\_}i}}\left\{a_x\pm t_{\text{w}}\dot{\varphi}\dot{\theta}-l_i\left(\dot{\theta}^2+\dot{\phi}^2\right)\right\}\\&\quad+\left(m_{\text{w}}+\frac{m_{\text{arm}}}{2}\right)\left[a_z\pm t_{\text{w}}\dot{\phi}\dot{\theta}+l_i\dot{\phi}\dot{\varphi}\right]+l_{\text{arm}}\left(m_{\text{w}}+\frac{m_{\text{arm}}}{4}\right)\cos(\theta_{\text{arm\_}i})\left\{\dot{\varphi}^2-\dot{\phi}^2\right\}\\&\quad+l_{\text{arm}}\left(m_{\text{w}}+\frac{m_{\text{arm}}}{4}\right)\frac{\cos^2(\theta_{\text{arm\_}i})-\sin^2(\theta_{\text{arm\_}i})}{\sin\theta_{\text{arm\_}i}}\dot{\phi}\dot{\varphi}\end{aligned} \tag{50}$$

In equation (50), first and second terms relate to the arm motion and the other terms are to the vehicle body's motion. Using equation (50), the vertical tyre force can be estimated as

$$\hat{F}_{\text{tz}i}(k)=F_{\text{tz}i\_\text{static}}+\sum_{i=0}^{N}\frac{\Delta\hat{F}_{\text{tz}i}(k-i\Delta T)}{N} \tag{51}$$

where $F_{\text{tz}i\_\text{static}}$ is a static vertical tyre force at the ith wheel.

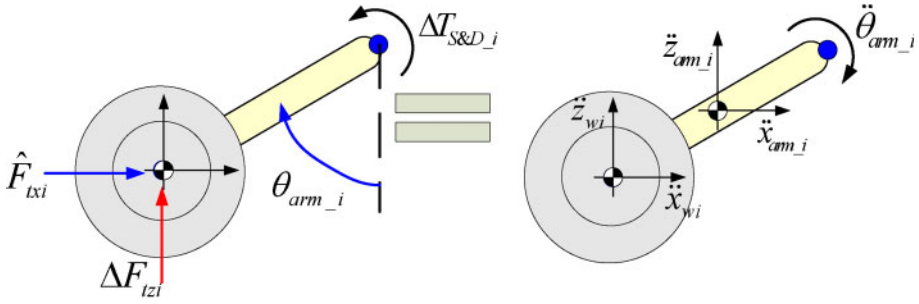

Fig. 14 Simplified arm dynamic model

5 SIMULATION RESULTS

Simulation studies in the autonomous driving control mode are conducted in order to evaluate the driving control algorithm based on skid steering. The dynamic model validated in section 2 is used for the simulation studies. In order to investigate the effects of slip control, the simulation results with slip control are compared with the simulation results without slip control in identical driving conditions as follows: the radius of the S curve trajectory, the desired trajectory, is 6 m; the tyre–road friction coefficient is 0.85; the desired speed is 8.5 km/h at constant; the initial speed of vehicle is 6 km/h; and the maximum slip ratio value is set at 0.2.

The simulation results in the autonomous control mode are presented in Fig. 15. Figure 15(a) shows the desired speed and the longitudinal vehicle speed. Vehicle yaw rates are presented in Fig. 15(b). Figures 15(c) and (d) show the lateral position error and yaw angle error. From Figs 15(c) and (d), it is found that the lateral position error and the yaw angle with slip control are less than half of the tracking performance with non-slip control. Vehicle trajectories are presented in Fig. 15(f). As shown in Figs 15(c), (d), and (f), the vehicle with slip control tracks the desired trajectory closer than that with non-slip control as well as having guaranteed vehicle stability, in contrast to that with non-slip control. Figure 15(e) shows the middle wheel slip ratio. The slip ratio without the slip control is as large as the wheel can run idle when the desired tyre force is required excessively, as shown in Fig. 15(e). On the other hand, if the control input for slip limitation is applied, it is possible to track the desired trajectory in the small slip ratio region and at the same time reduce the energy consumption of the in-wheel motor.

Figure 16 shows the estimated tyre force and wheel torque inputs of the middle wheel in the above simulation. The estimated tyre forces are required for the optimal tyre force distribution and the wheel slip control. The estimated longitudinal and vertical tyre forces are compared with the longitudinal and vertical tyre forces of the dynamic model as shown in Figs 16(a) and (b). From Figs 16(b) and (c), it can be found that the wheel torque input is determined in proportion to the estimated vertical tyre force.

In order to compare numerically the above simulation results, the performance indexes of the speed control, trajectory tracking control, and total energy consumption of in-wheel motors are defined as

$$J_{\text{speed\_control}} = \int (v_x - V_{\text{des}})^2 \, \mathrm{d}t \tag{52}$$

$$J_{\text{tracking\_performance}} = \int y_{\text{r}}{}^2 \, \mathrm{d}t \tag{53}$$

$$\text{Energy consumption} = \sum_{i=1}^{6} \int |T_i \omega_i| \, \mathrm{d}t \tag{54}$$

The performance indexes and the total energy consumption obtained using equations (52) to (54) are presented in Fig. 17. From Figs 15 and 17, it can be found that the slip control in the wheel torque controller should be considered in order to prevent unnecessary energy consumption at each wheel as well as to improve the vehicle motion control performance.

6 VEHICLE TEST RESULTS

Vehicle tests have been conducted in order to evaluate the proposed driving control algorithm for remote control manoeuvring and autonomous driving control. The tests were performed using the control system as shown in Fig. 18. Figure 18 shows a configuration diagram of the control system in this study. The control system consists of a remote

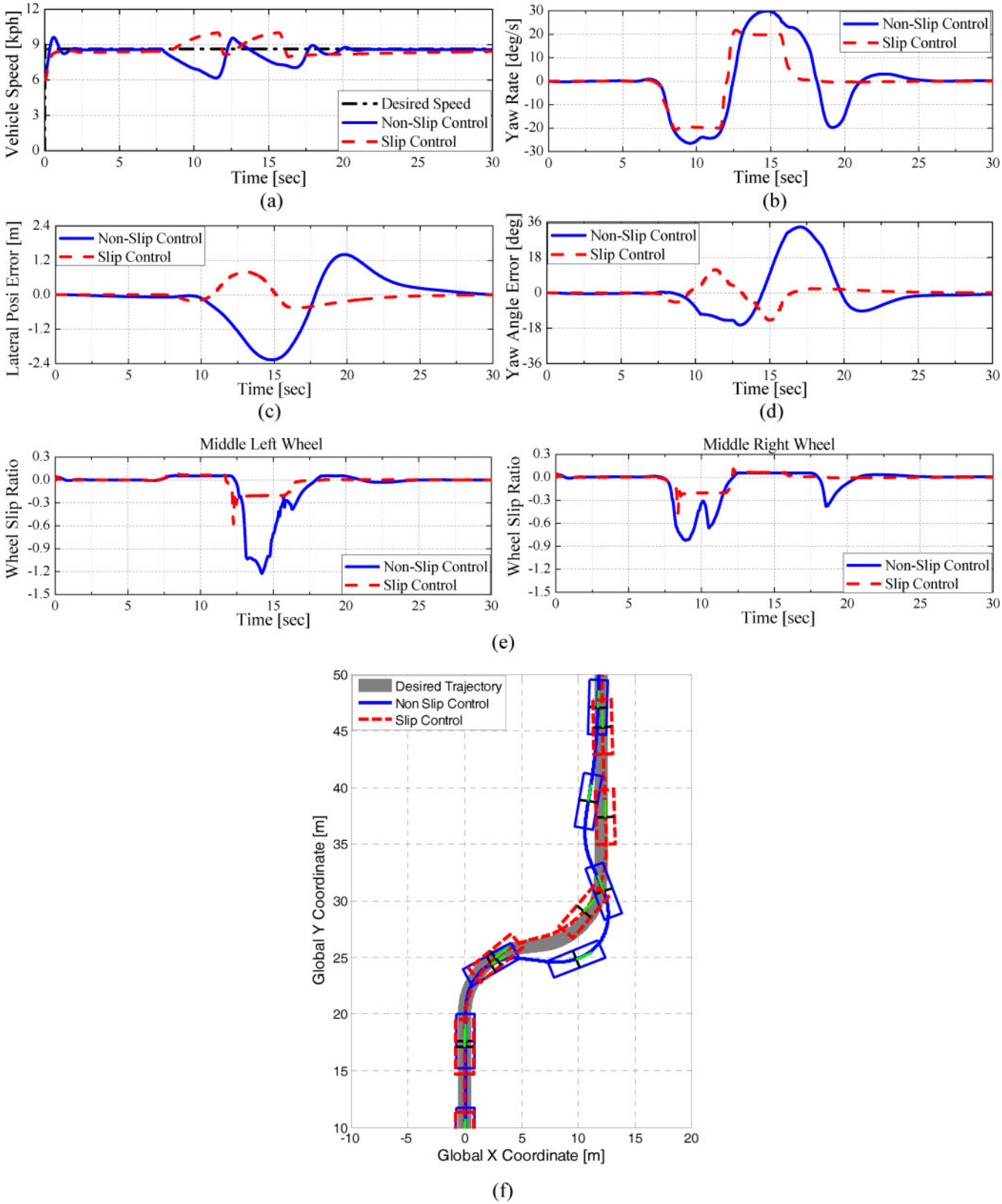

Fig. 15 Comparison of simulation results, non-slip control versus slip control: (a) vehicle speed (km/h), (b) yaw rate (deg/s), (c) lateral position error (m), (d) yaw angle error (deg), (e) slip ratio (middle wheel), and (f) vehicle trajectory

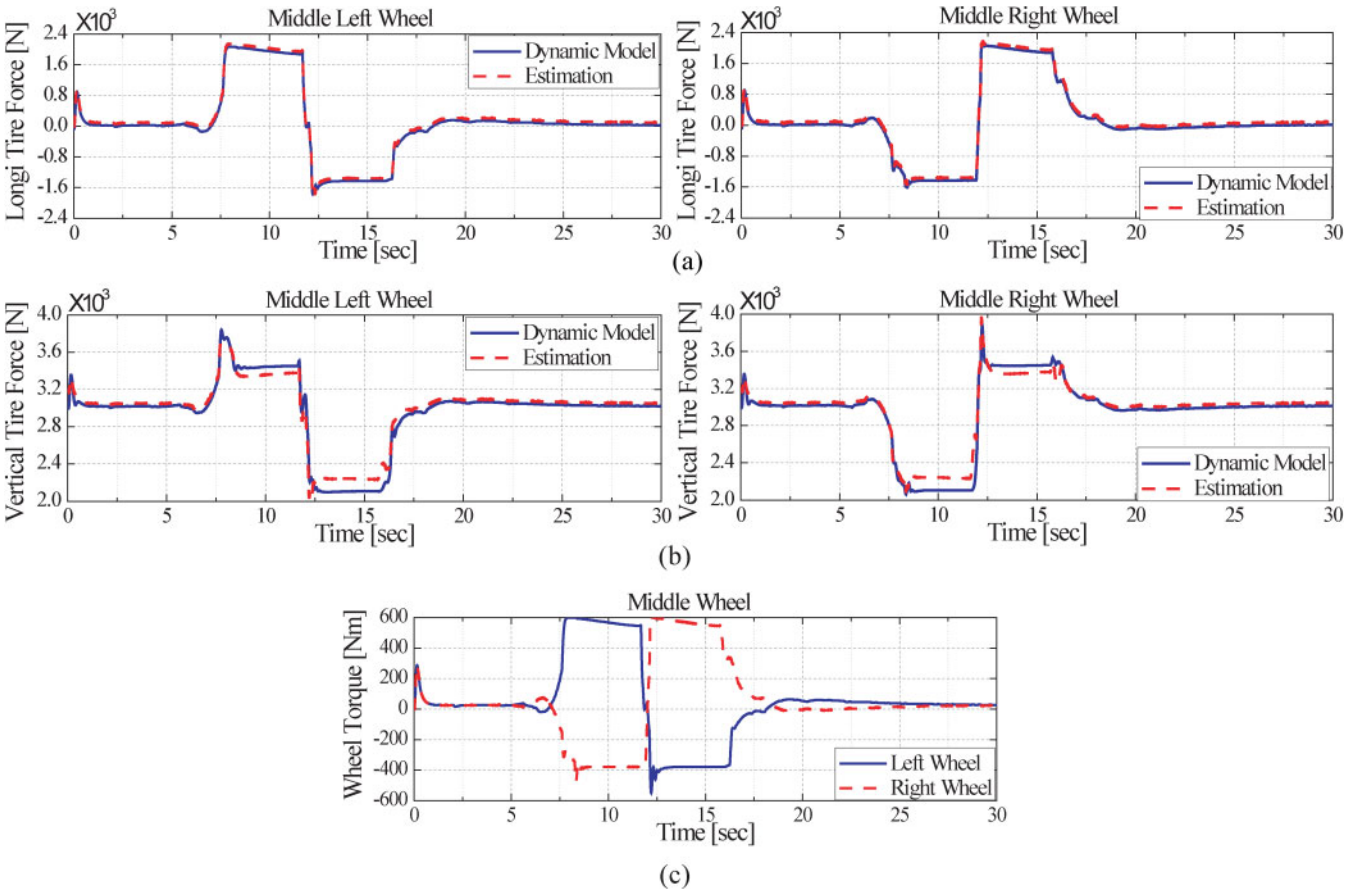

Fig. 16 Estimated tyre forces and wheel torque input: (a) estimated longitudinal tyre force (middle wheel) (N) (b) estimated vertical tyre force (middle wheel) (N), and (c) wheel torque input (middle wheel) (N m) controller

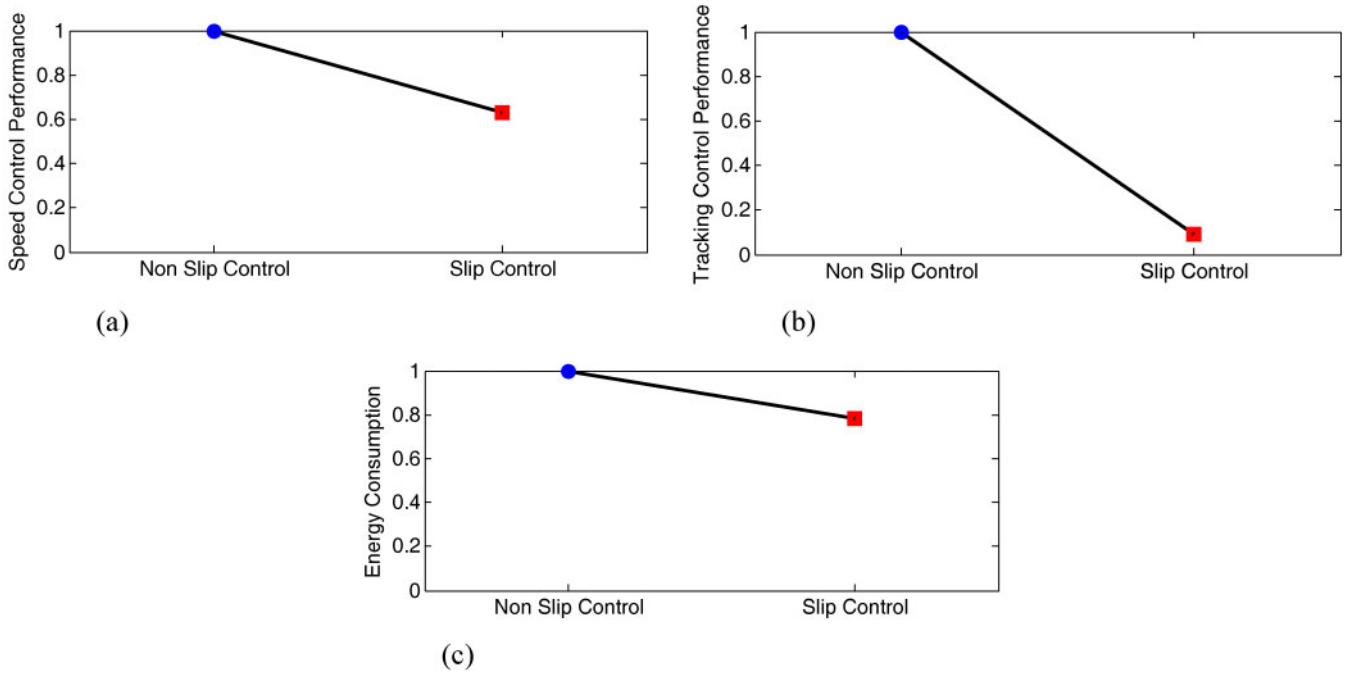

Fig. 17 Comparison of performance index, non-slip control versus slip control: (a) performance index of speed control, (b) performance index of trajectory tracking, and (c) energy consumption of in-wheel motor controller

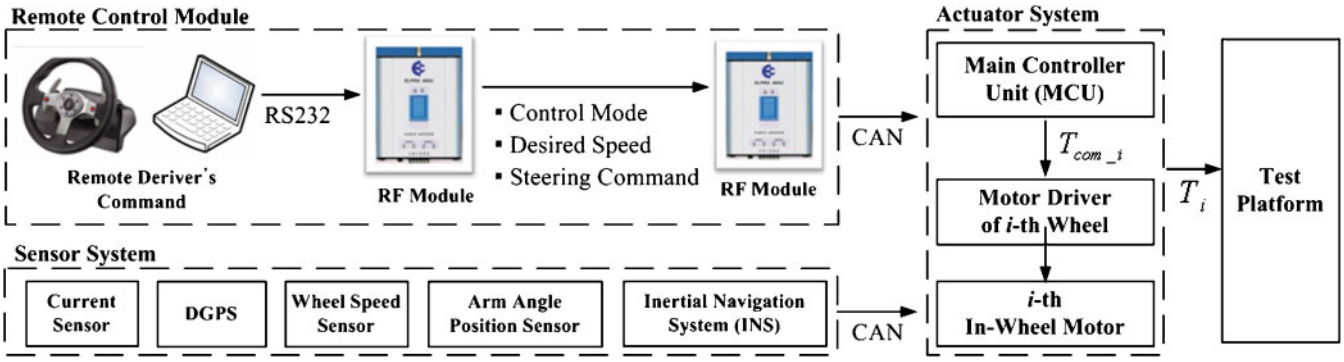

Fig. 18 Configuration of control system controller

control module, an actuator system, and a sensor system. The remote control module is used to communicate the remote driver's command control mode, desired speed, and steering command to the main controller unit. The driving controller developed in this paper is implemented on the main controller unit, in order to determine the wheel torque command. An ADTM-C6713 DSP module is used as the main controller unit. The driving controller runs with a sampling time of 10 ms on the main controller unit. The motor driver in the actuator system controls the in-wheel motor at each wheel in order to generate the wheel torque command. In the actuator system, the rated output of the in-wheel motor is 5 kW. The signals listed in Fig. 8 are measured using an inertial navigation system (INS), a differential global positioning system (DGPS), a current sensor, wheel speed sensor, and arm position sensor.

6.1 Remote control manoeuvring

Vehicle test results in a remote control manoeuvring mode are compared to the simulation results. Figure 19 shows a comparison of the vehicle test and simulation results. The simulation and vehicle tests are conducted in identical conditions as follows: the tyre–road friction coefficient is 0.85, the desired speed is 10 km/h at constant, the maximum wheel torque is 580 N m, and the maximum value of slip ratio is set to be 0.2.

From Fig. 19, it can be found that the vehicle test results agree closely with the simulation results. Figure 19(a) denotes the steering command determined by the remote driver in the vehicle test. The steering command is used to compute the desired yaw rate as shown in Fig. 19(c). Figure 19(b) shows the desired speed and the vehicle speed. The desired yaw rate and the actual yaw rate are presented in Fig. 19(c). As mentioned in section 2, in the case of the vehicle test, the yaw rate is fluctuated by the vertical road profile. Also, left and right yaw motion is unbalanced due to the offset of the mass centre of the test platform. However, even though there are some differences between simulation and test data, the yaw rate of the test data tends to track the desired yaw rate. The estimated longitudinal and vertical tyre forces in the vehicle test are compared with the longitudinal and vertical tyre forces of the dynamic model in Figs 19(d) and (e). It can be found from Figs 19(e) and (f) that the wheel torque input is determined in proportion to the estimated vertical tyre force.

6.2 Autonomous driving control

Autonomous trajectory tracking tests were conducted to evaluate the trajectory tracking controller, and the test results are shown in Fig. 20. The desired trajectory, as shown in Fig. 20(a), is defined as a digital map in order to calculate the lateral position error and the yaw angle error [**22**]. The vehicle test results are compared with the simulation results as shown in Fig. 20.

Figure 20(a) shows the desired trajectory and vehicle position obtained using DGPS. The DGPS is used to provide the absolute position and yaw angle of the test platform. The accuracies of the position and the yaw angle are 0.1 m and 0.5 degrees respectively. Figure 20(b) denotes the speed control performance. In the vehicle test, a desired speed is set to be 10 km/h. As mentioned earlier, the maximum power of each in-wheel motor is 5 kW. However, since the maximum power of the test platform is 25 kW, not all of the in-wheel motors can consume maximum power at once. This causes the speed control performance in the vehicle test to be lower than the simulation results, as shown in Fig. 20(b). The actual yaw rate in the vehicle test agrees closely with the simulation results as shown in Fig. 20(c). The trajectory tracking performance is

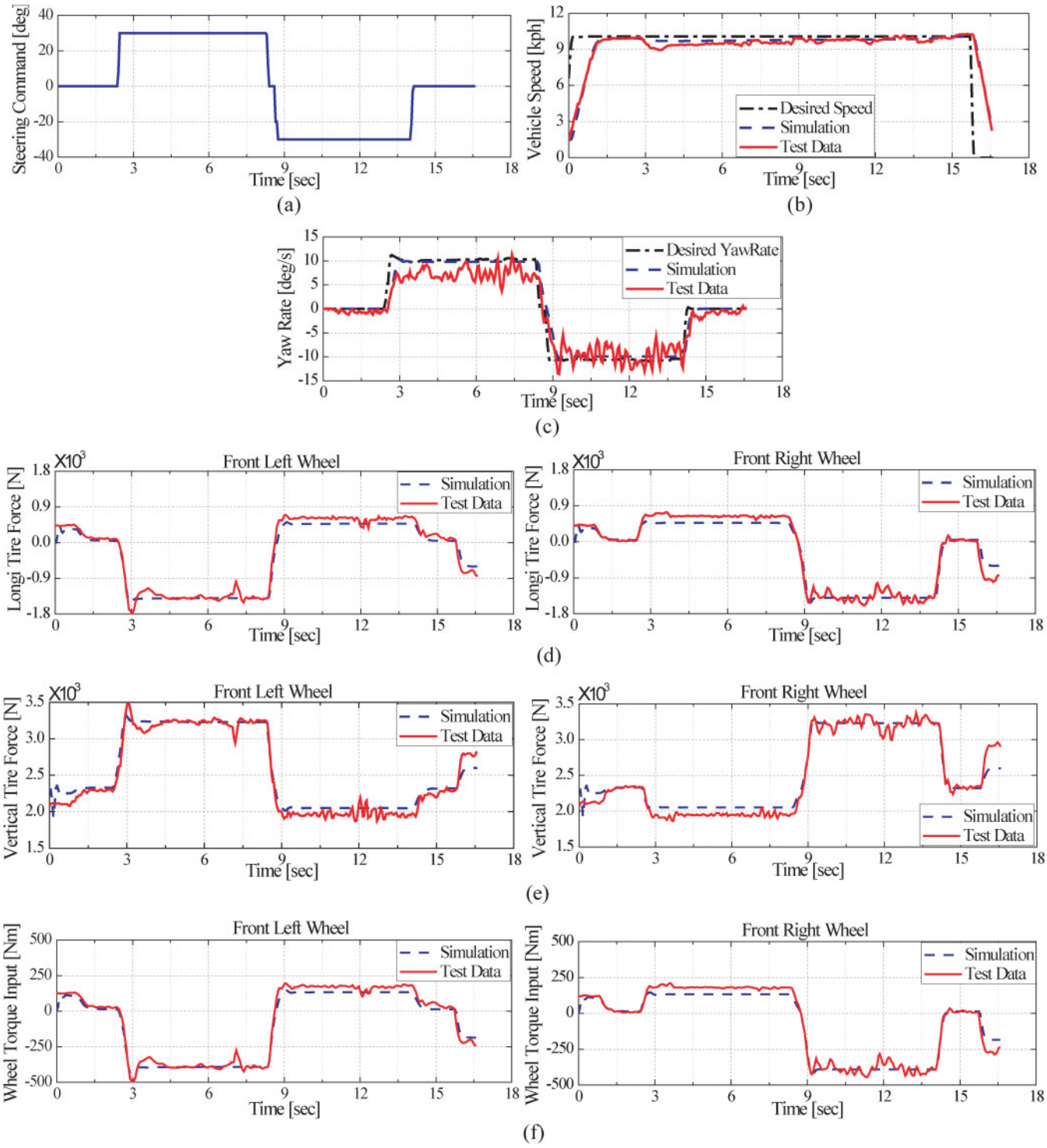

Fig. 19 Vehicle test results in remote control mode: (a) steering command (deg), (b) vehicle speed (km/h), (c) yaw rate (deg/s), (d) estimated longitudinal tyre force (front wheel) (N), (e) estimated vertical tire force (front wheel) (N), and (f) wheel torque input (front wheel) (N m)

presented in Figs 20(d) and (e). From these figures, it can be confirmed that the proposed trajectory tracking controller produces a satisfactory tracking performance, with the magnitudes of lateral and yaw angle error below 0.5 m and 3.0 degrees respectively. These errors are on the same order of magnitude as the errors predicted in the simulation. Finally, it can be confirmed that the wheel torque input is

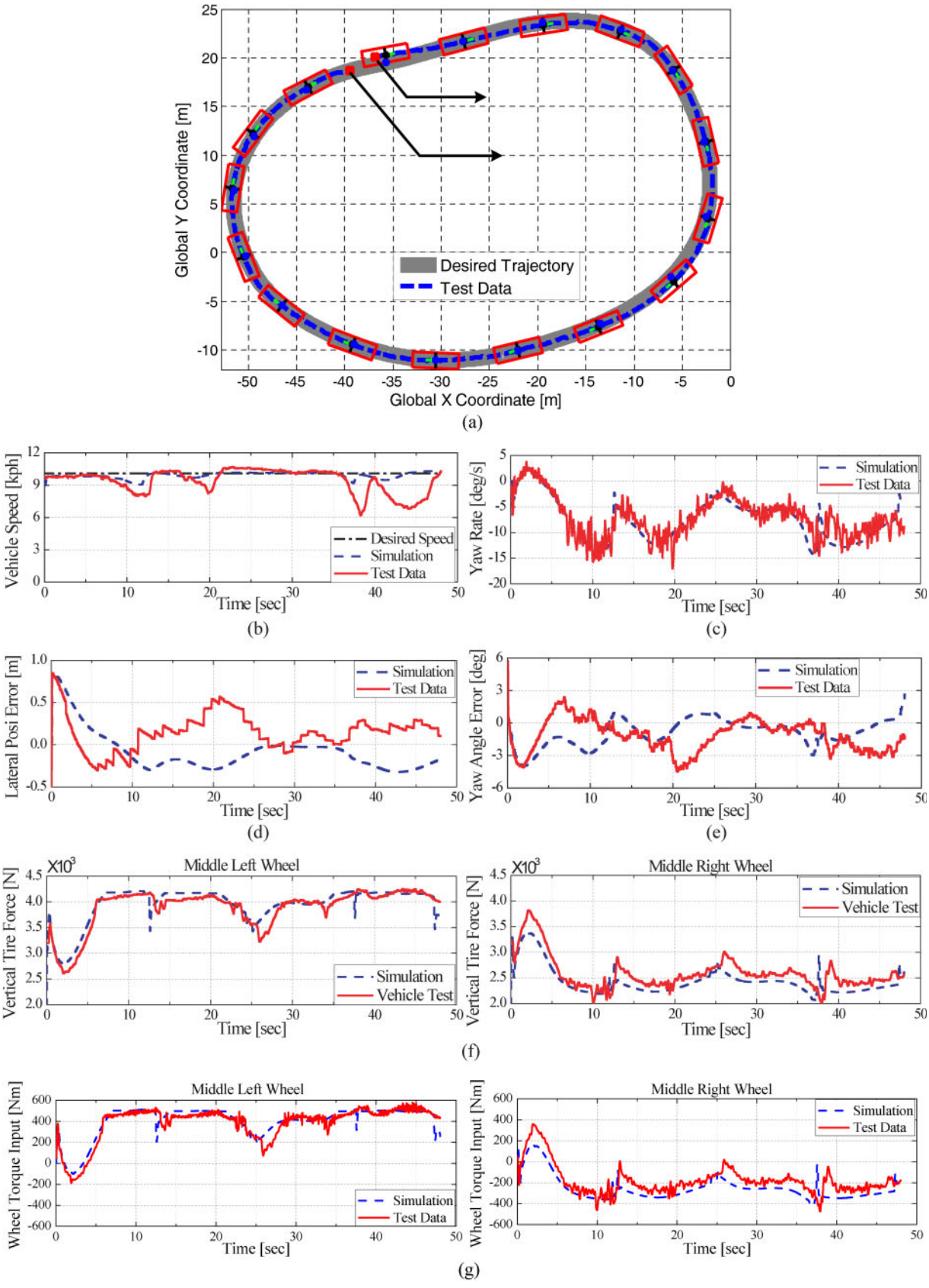

Fig. 20 Comparison of the simulation and test results: (a) desired trajectory and vehicle trajectory, (b) vehicle speed (km/h), (c) vehicle yaw rate (deg/s), (d) lateral position error (m), (e) yaw angle error (deg), (f) vertical tyre force (middle wheel) (N), and (g) wheel torque input (middle wheel) (N m)

determined in proportion to the estimated vertical tyre force as shown in Figs 20(f) and (g).

7 CONCLUSION

A skid steering-based driving control algorithm for a robotic vehicle with articulated suspension (RVAS) has been presented. A dynamic model for the RVAS has been developed and validated using test data. The driving control algorithm has been developed to control the vehicle motion according to a remote driver's command or to track a prescribed trajectory on a variety of rough terrains. The proposed driving control algorithm has been evaluated through numerical simulations and vehicle tests.

The driving controller consists of an upper- and lower-level controller. The upper-level controller has been developed to compute a total traction force and a yaw moment input according to the control modes: the remote control manoeuvring mode and an autonomous driving control mode. In the remote control manoeuvring mode, the yaw moment input is calculated using the sliding control method in order to reduce the yaw rate error between the desired yaw rate and the actual yaw rate. In the autonomous driving control mode, the yaw moment input is determined to track a prescribed trajectory. The tracking controller for trajectory tracking has been designed using the optimal finite preview control method.

The lower-level controller was designed to determine a wheel torque command at each wheel in order to apply the upper-level control inputs to a test platform. The lower-level controller consists of a tyre force distribution algorithm and a wheel torque controller. In the tyre force distribution algorithm, a desired longitudinal tyre force of each wheel is computed using the estimated vertical tyre force. The wheel torque controller determines the wheel torque command using the desired longitudinal tyre force and the estimated longitudinal tyre force in order to keep a slip ratio at each wheel below a limit value as well as to track the desired longitudinal tyre force.

The longitudinal and vertical tyre forces were estimated for the optimal tyre force distribution and the wheel slip control. The estimated longitudinal tyre forces were obtained using the estimated wheel angular acceleration and the wheel dynamics. The vertical tyre forces were estimated using the estimated longitudinal tyre force based on the arm dynamics.

Simulation studies and vehicle tests were conducted in order to evaluate the proposed driving control algorithm. From the simulation and test results, it was found that the proposed driving controller computes the suitable wheel torque command to track the desired speed and desired yaw rate or desired trajectory according to the control mode. It was shown that the proposed driving controller provides good manoeuvrability. As future work, vehicle tests will be conducted on a variety of rough terrains using the proposed driving control algorithm.

ACKNOWLEDGEMENTS

This work was supported by the Samsung Techwin, the BK 21 Program, the SNU-IAMD, the Korea Research Foundation Grant funded by the Korean Government (MEST) (KRF-2009-200-D00003), National Research Foundation of Korea Grant funded by the Korean Government (2009-0083495) and the Agency to Defense Development.

REFERENCES

1 **Golconda, S.** *Steering controller for a skid-steered autonomous ground vehicle at varying speed.* PhD Thesis, Osmania University, India, 2005.
2 **Economou, J. T.** and **Colyer, R. E.** Modelling of skid steering and fuzzy logic vehicle ground interaction. In Proceedings of the American Control Conference, Chicago, Illinois, 28–30 June 2000, vol. 1, pp. 100–104.
3 **Dixon, W. E., Dawson, D. M., Zergeroglu, E.,** and **Behal, A.** Nonlinear control of wheeled mobile robots. In *Lecture notes in control and information sciences,* vol. 262, 2001 (Springer-Verlag, London).
4 **Cho, W., Yoon, J., Kim, J., Hur, J.,** and **Yi, K.** An investigation into unified chassis control scheme for optimized vehicle stability and maneuverability. *Veh. Syst. Dyn.*, 2008, **46**(Suppl.), 87–105.
5 **Yi, K., Chung, T., Kim, J.,** and **Yi, S.** An investigation into differential braking strategies for vehicle stability control. *Proc. IMechE, Part D: J. Automobile Engineering*, 2003, **217**, 1081–1093. DOI: 10.1243/09544070JAUTO77.
6 **Uematsu, K.** and **Gerdes, J. C.** A comparison of several sliding surfaces for stability control. In Proceedings of the 6th International Symposium on *Advanced vehicle control (AVEC2002)*, Hiroshima, Japan, 2002.
7 **Chen, B.** and **Peng, H.** Differential-braking-based rollover prevention for sport utility vehicles with human-in-the-loop evaluations. *Veh. Syst. Dyn.*, **36**(4–5), 359–389.
8 **Kang, J., Hindiyeh, R. Y., Moon, S., Gerdes, J. C.,** and **Yi, K.** Design and testing of a controller for autonomous vehicle path tracking using GPS/INS sensors. In Proceedings of the 17th World Con-

gress, The International Federation of Automatic Control, pp. 2093–2098, 2008.
9 **Peng, H.** *Vehicle lateral control for highway automation*. PhD Thesis, University of California at Berkeley, 1992.
10 **Lenain, R., Thuilot, B., Cariou, C.,** and **Martinet, P.** Adaptive control for car-like vehicles guidance relying on RTK GPS: rejection of sliding effects in agricultural applications. In Proceedings of the 2003 IEEE International Conference on *Robotics and automation*, September 2003, vol. 1, pp. 115–120.
11 **Lizarralde, F., Nunes, E., Hsu, L.,** and **Wen, J.** Mobile robot navigation using sensor fusion. In Proceedings of the 2003 IEEE International Conference on *Robotics and automation*, vol. 1, September 2003, pp. 458–463.
12 **Rajamani, R.** *Vehicle dynamics and control*, 2006, pp. 387–432 (Springer, New York).
13 **Jazar, R. N.** *Vehicle dynamics: theory and application*, 2008, pp. 220–303 (Springer).
14 **Kang, J., Kim, W., Jung, S.,** and **Yi, K.** Skid steering based maneuvering of robotic vehicle with articulated suspension. *SAE Int. J. Passeng. Cars-Mech. Syst.*, 2009, **2**(1), 645–652.
15 **Visioli, A.** Modified anti-windup scheme for PID controllers. In Proceedings of the Control Theory and Applications Conference, January 2003, vol. 150, pp. 49–54.
16 **Cho, W., Yoon, J., Yim, S., Koo, B.,** and **Yi, K.** Estimation of tire forces for application to vehicle stability control. *IEEE Transactions on Vehicular Technology* (in press).
17 **Ray, L. R.** Non-linear tyre force estimation and road friction identification: simulation and experiments. *Automatica*, 1997, **33**(10), 1819–1833.
18 **Rajamani, R., Piyabongkarn, D., Lew, J. Y.,** and **Grogg, J. A.** Algorithms for real time estimation on individual wheel tire-road friction coefficients. In Proceedings of the 2006 American Control Conference, 2006, pp. 4682–4687.
19 **Mokhiamar, O.** and **Abe, M.** Simultaneous optimal distribution of lateral and longitudinal tire forces for the model following control. *ASME, J. Dyn. Syst. Measmt. Contr.*, 2004, **126**, 753–763.
20 **Buckholtz, K. R.** Reference input wheel slip tracking using sliding mode control. In Proceedings of the SAE World Congress and Exhibition, Detroit, Michigan, 2002, SAE paper 2002-01-0301.
21 **Zhang, Q., Liu, G., Wang, Y.,** and **Zhou, T.** A study of calculation method of wheel angular acceleration in ABS system. In Proceedings of 2004 International Conference on *Information acquisition*, June 2004, pp. 147–150.
22 **Rossetter, E. J., Switkes, J. P.,** and **Gerdes, J. C.** A gentle nudge towards safety: experimental validation of the potential field driver assistance system. In Proceedings of the 2003 American Control Conference, 4–6 June 2003, pp. 3744–3749.

APPENDIX

Notation

c_{d}	rotational damping coefficient of the arm rod
$F_{\mathrm{s}xi}$	longitudinal internal force acting on a sprung mass at the rotational centre of the ith arm rod
$F_{\mathrm{s}yi}$	lateral internal force acting on a sprung mass at the rotational centre of the ith arm rod
$F_{\mathrm{s}zi}$	vertical internal force acting on a sprung mass at the rotational centre of the ith arm rod
$F_{\mathrm{t}xi}$	longitudinal tyre force at the ith wheel
$F_{\mathrm{t}yi}$	lateral tyre force at the ith wheel
$F_{\mathrm{t}zi}$	vertical tyre force at the ith wheel
F_{x_des}	total traction force
$\hat{F}_{\mathrm{t}xi}$	estimated longitudinal tyre force of the ith wheel
$\hat{F}_{\mathrm{t}zi}$	estimated vertical tyre force of the ith wheel
g	gravity acceleration
I_{arm_x}	moment of inertia of the arm rod about the roll axis
I_{arm_y}	moment of inertia of the arm rod about the pitch axis
I_{arm_z}	moment of inertia of the arm rod about the yaw axis
I_x	moment of inertia of the vehicle about the roll axis
I_y	moment of inertia of the vehicle about the pitch axis
I_z	moment of inertia of the vehicle about the yaw axis
J_{w}	moment of inertia of the in-wheel motor
k_{s}	rotational spring stiffness of the arm rod
l_{arm}	length of the arm rod
l_{f}	distance from the centre of gravity (c.g.) to the front arm axle
l_{m}	distance from the c.g. to the middle arm axle
l_{r}	distance from the c.g. to the rear arm axle
l_{wf}	distance from the c.g. to the front wheel axle
l_{wm}	distance from the c.g. to the middle wheel axle

l_{wr}	distance from the c.g. to the rear wheel axle
m	vehicle mass
m_{arm}	mass of the arm rod
m_s	sprung mass of vehicle
m_w	mass of in-wheel motor
M_{sxi}	internal moment acting on the sprung mass about the roll axis at the rotational centre of the ith arm rod
M_{szi}	internal moment acting on the sprung mass about the yaw axis at the rotational centre of the ith arm rod
M_{z_des}	yaw moment input
$\dot{r}_{cg}$	vehicle velocity vector
$\ddot{r}_{cg}$	vehicle translational acceleration vector
γ_d	desired yaw rate
$\ddot{r}_i$	translational acceleration vector of the rotational centre of the ith arm rod
$\ddot{r}_{wi}$	translational acceleration vector of the ith wheel
R_i	tyre radius of the ith wheel
t_w	half of tread (half of track width)
T_{com_i}	torque command of the ith in-wheel motor
T_i	measured wheel torque of the ith wheel
T_{self_i}	self-aligning torque at the ith wheel
$T_{S\&D\_i}$	sum of spring and damping torques of the ith arm rod
v_x	vehicle longitudinal velocity
v_y	vehicle lateral velocity
v_z	vehicle vertical velocity
V_{des}	longitudinal desired speed
X_i	desired longitudinal tyre force of the ith wheel
y_r	lateral position error
α_i	slip angle at the ith wheel
α_{cg}	vehicle angular acceleration vector
α_{arm_i}	angular acceleration vector of the ith arm rod
δ_{com}	remote driver's steering command
$\dot{\theta}$	pitch rate
θ_{arm_i}	arm angle at ith arm rod
θ_{arm_static}	static arm angle
λ_i	slip ratio at the ith wheel
λ_{max}	maximum slip ratio
$\dot{\phi}$	roll rate
φ_d	desired yaw angle
$\dot{\varphi}$	yaw rate
ω_{arm_i}	angular velocity vector of the ith arm rod
ω_{cg}	vehicle angular velocity vector
ω_i	wheel angular speed at the ith wheel
ω_{i_des}	desired angular speed of the ith wheel
$\hat{\dot{\omega}}_i(k)$	estimated angular acceleration of the ith wheel